REPORT DOCUMENTATION PAGE

Form Approved OMB NO. 0704-0188

1. REPORT DATE (DD-MM-YYYY) 05-02-2016	2. REPORT TYPE MS Thesis	3. DATES COVERED (From - To) -

4. TITLE AND SUBTITLE
Femtosecond Nonequilibrium Carrier Dynamicsin CdMgTe Single Crystals

5a. CONTRACT NUMBER
W911NF-12-2-0076

5b. GRANT NUMBER

5c. PROGRAM ELEMENT NUMBER
611102

6. AUTHORS
Fei Xia Song

5d. PROJECT NUMBER

5e. TASK NUMBER

5f. WORK UNIT NUMBER

7. PERFORMING ORGANIZATION NAMES AND ADDRESSES
University of Rochester
ORPA
518 Hylan Building
Rochester, NY 14627 -0140

8. PERFORMING ORGANIZATION REPORT NUMBER

9. SPONSORING/MONITORING AGENCY NAME(S) AND ADDRESS (ES)
U.S. Army Research Office
P.O. Box 12211
Research Triangle Park, NC 27709-2211

10. SPONSOR/MONITOR'S ACRONYM(S)
ARO

11. SPONSOR/MONITOR'S REPORT NUMBER(S)
60296-EL.7

12. DISTRIBUTION AVAILIBILITY STATEMENT
Approved for public release; distribution is unlimited.

13. SUPPLEMENTARY NOTES
The views, opinions and/or findings contained in this report are those of the author(s) and should not contrued as an official Department of the Army position, policy or decision, unless so designated by other documentation.

14. ABSTRACT

CdMgTe (CMT) is regarded as one of the most promising alternative material used for radiation detector instead of CdZnTe. CMT has many advantages such as high resistivity, good electron-mobility product, high effective mass and high density. For photoelectronic applications, it is quite important to understand the CMT optical photoresponse and its dynamics, as well as the main relaxation channels of photoexcited carriers. In in this thesis, femtosecond pump-probe spectroscopy is used to study the ultrafast photoresponse and nonequilibrium carrier dynamics in CMT, and information of carrier dynamics is obtained by modeling the measured waveforms, using a

15. SUBJECT TERMS
Ultrafast phenomena, CdMgTe Single Crystals, terahertz photoresponse, photoconductive detectors

16. SECURITY CLASSIFICATION OF:			17. LIMITATION OF ABSTRACT	15. NUMBER OF PAGES	19a. NAME OF RESPONSIBLE PERSON Roman Sobolewski
a. REPORT	b. ABSTRACT	c. THIS PAGE			
UU	UU	UU	UU		19b. TELEPHONE NUMBER 585-275-1551

Standard Form 298 (Rev 8/98)
Prescribed by ANSI Std. Z39.18

Report Title

Femtosecond Nonequilibrium Carrier Dynamicsin CdMgTe Single Crystals

ABSTRACT

CdMgTe (CMT) is regarded as one of the most promising alternative material used for radiation detector instead of CdZnTe. CMT has many advantages such as high resistivity, good electron-mobility product, high effective mass and high density. For photoelectronic applications, it is quite important to understand the CMT optical photoresponse and its dynamics, as well as the main relaxation channels of photoexcited carriers. In in this thesis, femtosecond pump-probe spectroscopy is used to study the ultrafast photoresponse and nonequilibrium carrier dynamics in CMT, and information of carrier dynamics is obtained by modeling the measured waveforms, using a set of differential rate equations. In CMT single crystals, carriers get photoexcited on femtosecond time scale through two mechanisms, standard valence band-conduction band excitation, and excitation into the conduction band of trapped electrons. It turns out that traps play the crucial role in CMT photoresponse. After excitation, carriers go through trapping, electron-phonon scattering, and recombination. The dominant is trapping with the trap-time of ~200 fs, while the recombination time is ~5 ps. Finally, Electron-phonon interaction is the least probable process and becomes relevant only for high intensity photon pumping.

Femtosecond Nonequilibrium Carrier Dynamics in CdMgTe Single Crystals

By

Fei Song

Submitted in Partial Fulfillment of the

Requirements for the Degree

Master of Science

Supervised by Professor Roman Sobolewski

Materials Science Program

Arts, Science and Engineering

Edmund A. Hajim School of Engineering and Applied Sciences

University of Rochester

Rochester, New York

2015

Biographical Sketch

Fei Song [redacted]. She attended Shenzhen University in China from 2008-2012 where she earned a Bachelor of Science degree in Materials Science. Begining in the fall of 2013, Fei began studying at the University of Rochester in pursuit of a Master of Science degree in Materials Science with a concentration in Semiconductor Materials. She persued her research on the ultrafast carrier dynamics in CMT single crystals under the supervision of Professor Roman Sobolewski.

Acknowledgments

First and foremost, I would like to thank my adviser, Professor Roman Sobolewski, for his guidance in the development of this thesis. I learned very much while under his tutelage, and this work could not have been completed without him.

Also, I would like to thank John Serafini and Jie Zhao for their immense help in learning the pump-probe system and for their helpful and productive discussions. With their thorough instruction I was able to successfully perform pump-probe measurements independently.

I would like to thank Yunus Akbas for his help in learning the Matlab software and in simulation analysis. With his patient instruction I finally understand how the software works and how to optimize the codes and requirements.

Finally, I would like to thank Anton Koroliov for his helpful suggestions and conversations.

Abstract

CdMgTe (CMT) is regarded as one of the most promising alternative material used for radiation detector instead of CdZnTe. CMT has many advantages such as high resistivity, good electron-mobility product ($\mu\tau_e$), high effective mass and high density. For photoelectronic applications, it is quite important to understand the CMT optical photoresponse and its dynamics, as well as the main relaxation channels of photoexcited carriers. In in this thesis, femtosecond pump-probe spectroscopy is used to study the ultrafast photoresponse and nonequilibrium carrier dynamics in CMT, and information of carrier dynamics is obtained by modeling the measured waveforms, using a set of differential rate equations. In CMT single crystals, carriers get photoexcited on femtosecond time scale through two mechanisms, standard valence band-conduction band excitation, and excitation into the conduction band of trapped electrons. It turns out that traps play the crucial role in CMT photoresponse. After excitation, carriers go through trapping, electron-phonon scattering, and recombination. The dominant is trapping with the trap-time of ~200 fs, while the recombination time is ~5 ps. Finally, Electron-phonon interaction is the least probable process and becomes relevant only for high intensity photon pumping.

Contributors and Funding Sources

This research was performed under Professor Roman Sobolewski of the Department of Electrical and Computer Engineering. All of the supplies and equipment utilized in this thesis were funded through the Laboratory for Laser Energetics with the exception of the studied CdMgTe samples which were grown by the Brookhaven National Laboratory (NY 11973, USA). The MIRA-VERDI femtosecond laser system is a part of the ARO Grant NO. W11NF-12-2-0076 research program.

Table of Contents

List of Figures

List of Tables

List of symbols

$\mu\tau_e$	mobility lifetime product
Z	effective atomic number
c	speed of light
L	laser cavity length
$\Delta R / R$	differential reflectivity
Δn	refrective index change
$\varepsilon_0\varepsilon_b$	background dielectric function
e	unit electronic charge
ω	probe angular frequency
m^*	effective mass of electrons in conduction band
R	prove beam original reflectivity
N_C	concentration of electrons in the bottom of the conduction band
N	concentration of photo-excited electrons
N_{trap}	concentration of trapped electrons
$N_{trap,final}$	concentration of final trapped electrons
$N_{trap,\max}$	maximum concentration of the trap sites in the sample
n	concentration of hot electrons
I	pump beam intensity
α	band-to-band absorption coefficient
β	two-photon-absorption coefficient
γ	trap-to-hot pumping coefficient

τ_p	full-width-at-half-maximum of the laser pulsse
τ_{cool}	cooling time of electrons
τ_{trap}	trap-time of electrons
$\tau_{trap,\max}$	the longest trap time of electrons
$\tau_{trap,\min}$	the shortest trap time of electrons
$\tau_{trap,con}$	trap-time of electrons initially at the bottom of conduction band
$\tau_{trap,hot}$	trap-time of electrons in the hot state
τ_{rec}	electron-hole recombination time

Chapter 1:Introduction

1.1 Basic information on Cadmium Magnesium Telluride

Cadmium magnesium telluride ($Cd_{1-x}Mg_xTe$; CdMgTe; CMT) is a ternary semiconductor compound of the group II-VI. The bandgap of CdMgTe can be tuned by changing the Mg composition. The bandgap follows the empirical equation：

$$Eg(x) = 1.52 + 1.7x \quad , \tag{1}$$

where x refers to the content of magnesium. CMT has been regarded as one of the most promising materials for radiation detectors, because of its proper bandgap, high mobility lifetime product ($\mu\tau_e$) and very high stopping power of Te atoms.

In general, II-VI semiconductors have several advantages for radiation detection applications, such as broad range of bandgaps (from 0.15 eV for HgTe to 4.4 eV for MgS), high effective mass, and relative ease of growing in ternary and quaternary forms, such as the CMT [1]. CMT shares the same cubic zincblende lattice structure with CdTe, which is heavily researched as heterostructures of CdMgTe/CdTe, and applied in optoelectronics or spintronics.

1.2 Radiation Detectors

All radiation detectors collect charged particles such as electrons, produced by photon interaction with the detector material. The detector material is determined mostly based on the energy range of interest. CMT has its most potential expected for X-ray or γ-ray detection. X-ray and γ-ray interact with matter through 3 mechanisms: the photoelectric effect, the Compton effect, and electron-positon pair production. The photoelectric effect is the most dominant effect among them, because a Compton scattered photon or an electron-positon pair would escape from the detection volume, their energy could not be collected.[1]

There are several important parameters for semiconductor radiation detectors. The first one is bandgap. A relatively large bandgap requires more energetic photons to create photogenerated carriers, and, thus, increases signal accuracy. While very small bandgap would prompt thermal excitations and correspondingly higher conductivity, resulting in the large dark current and noisy signal collection. The bandgap of interest for room temperature detectors is of the range from 1.35 to 2.55eV. [3-6] The electron and hole mobilities are also an important property to radiation detectors. High carrier mobilities ensure that the excited electrons and holes can drift out from the medium quickly so that it would not cause signal overlapping, and thus maintain optimal signal and data quality. Two parameters directly related to the collection efficiency of a detector are carrier lifetime and crystal quality. If the carrier lifetime is too short, carriers recombine immediately and cannot be collected. If there are too many traps or defects in the material crystalline structure, a lot of excited electrons are trapped and cannot be collected. Good radiation detector materials require long carrier lifetime and excellent crystal quality. [2]

Another parameter is atomic effective number, directly related to the excitation mechanism. For a given compound, let N to be the number of atoms per unit volume and Z its effective atomic number. The interaction cross-sections vary as NZ^5 for the photoelectric effect, NZ for Compton scattering, and NZ^2 for pair production. So high Z increases the energy range over which total energy absorption can occur due to the photoelectric effect.[1] For compound semiconductor detectors, the absorption efficiency is determined by the atomic density of the highest atomic number element in the materials, rather than the average Z value of the compounds.

There are three compounds that are currently most common for radiation detectors: gallium arsenide (GaAs), cadmium telluride (CdTe), and cadmium zinc telluride (CdZnTe; CZT). GaAs was the first compound semiconductor to demonstrate high resolution for γ-rays at room temperature[7], and was, subsequently, developed, principally, for X-ray imaging applications. GaAs has many desirable properties such as moderately wide bandgap (1.42 eV) and relatively high charge carrier mobility. Also, it has the potential for integrated microelectronic devices.[8] However, the materials that currently dominate in compound semiconductor radiation detectors are the CZT and CdTe systems. They both have higher average atomic number and wider bandgap than GaAs (Table 1). CdTe detectors usually suffer from poor hole collection, which leads to position-dependent charge collection for large devices. But cooled devices demonstrate improved resolution [9]. The induced charge can be adjusted primarily from electron transport and by a suitable design and biasing of a hemisphere-type detector. For CZT, addition of Zn reduces the dislocation density and produces crystals of higher structural quality. This material exhibits higher sensitivity to γ-rays than CdTe [10]. Unfortunately, thicker CZT detectors also suffer from insufficient hole collections as the CdTe detectors, that results in the shifting of γ-ray pulse height spectra towards lower energies. Several techniques have been developed in order to reduce position-dependent charge collection effects in CZT, such as pulse processing techniques and single-charge-carrier-sensing devices.[8] Table 1 lists the physical properties of some compound semiconductors.

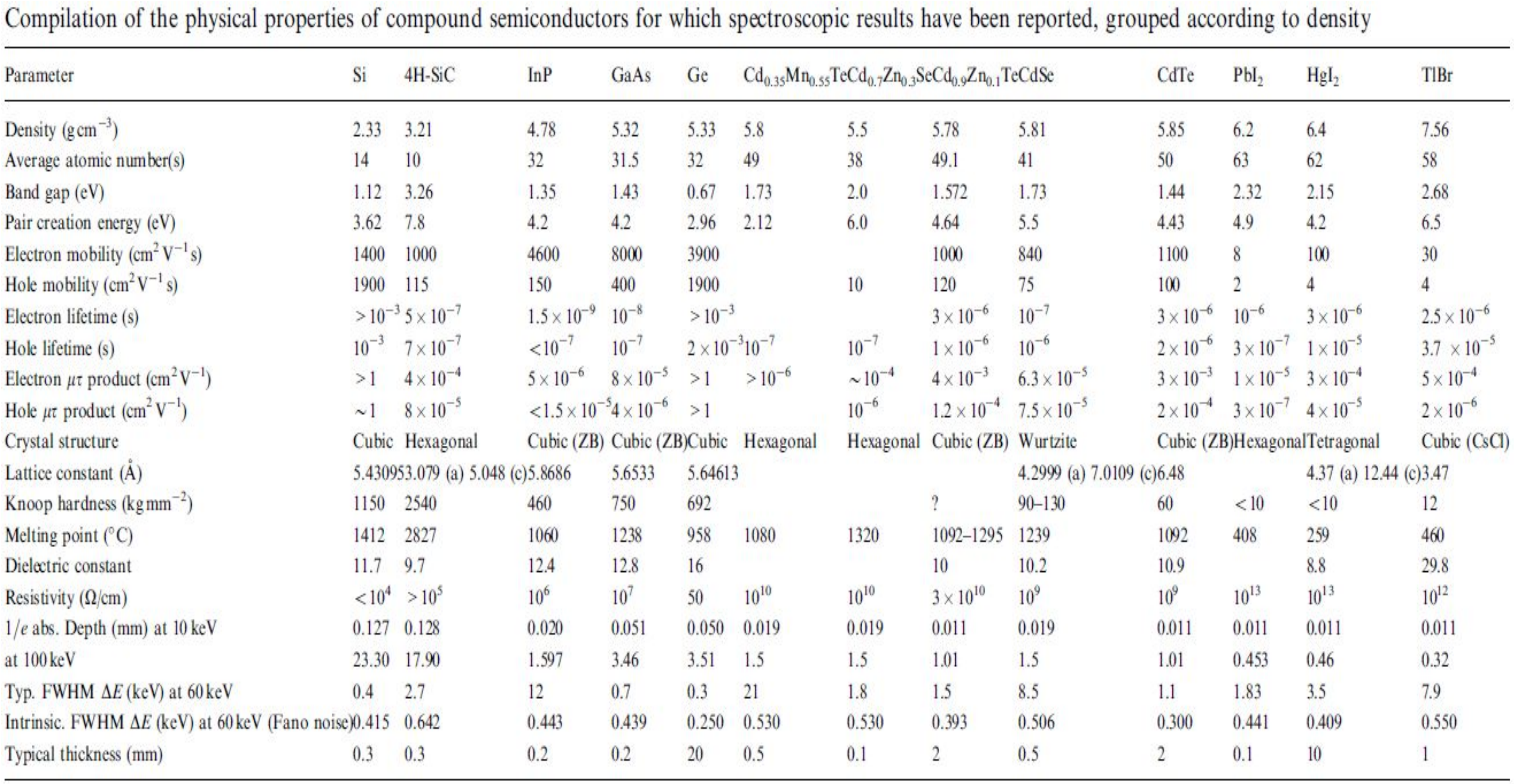

Compilation of the physical properties of compound semiconductors for which spectroscopic results have been reported, grouped according to density

Parameter	Si	4H-SiC	InP	GaAs	Ge	$Cd_{0.35}Mn_{0.55}Te$	$Cd_{0.7}Zn_{0.3}Se$	$Cd_{0.9}Zn_{0.1}Te$	CdSe	CdTe	PbI_2	HgI_2	TlBr
Density ($g\,cm^{-3}$)	2.33	3.21	4.78	5.32	5.33	5.8	5.5	5.78	5.81	5.85	6.2	6.4	7.56
Average atomic number(s)	14	10	32	31.5	32	49	38	49.1	41	50	63	62	58
Band gap (eV)	1.12	3.26	1.35	1.43	0.67	1.73	2.0	1.572	1.73	1.44	2.32	2.15	2.68
Pair creation energy (eV)	3.62	7.8	4.2	4.2	2.96	2.12	6.0	4.64	5.5	4.43	4.9	4.2	6.5
Electron mobility ($cm^2\,V^{-1}\,s$)	1400	1000	4600	8000	3900			1000	840	1100	8	100	30
Hole mobility ($cm^2V^{-1}\,s$)	1900	115	150	400	1900		10	120	75	100	2	4	4
Electron lifetime (s)	$>10^{-3}$	5×10^{-7}	1.5×10^{-9}	10^{-8}	$>10^{-3}$			3×10^{-6}	10^{-7}	3×10^{-6}	10^{-6}	3×10^{-6}	2.5×10^{-6}
Hole lifetime (s)	10^{-3}	7×10^{-7}	$<10^{-7}$	10^{-7}	2×10^{-3}	10^{-7}	10^{-7}	1×10^{-6}	10^{-6}	2×10^{-6}	3×10^{-7}	1×10^{-5}	3.7×10^{-5}
Electron $\mu\tau$ product (cm^2V^{-1})	>1	4×10^{-4}	5×10^{-6}	8×10^{-5}	>1	$>10^{-6}$	$\sim10^{-4}$	4×10^{-3}	6.3×10^{-5}	3×10^{-3}	1×10^{-5}	3×10^{-4}	5×10^{-4}
Hole $\mu\tau$ product ($cm^2\,V^{-1}$)	~1	8×10^{-5}	$<1.5\times10^{-5}$	4×10^{-6}	>1		10^{-6}	1.2×10^{-4}	7.5×10^{-5}	2×10^{-4}	3×10^{-7}	4×10^{-5}	2×10^{-6}
Crystal structure	Cubic	Hexagonal	Cubic (ZB)	Cubic (ZB)	Cubic	Hexagonal	Hexagonal	Cubic (ZB)	Wurtzite	Cubic (ZB)	Hexagonal	Tetragonal	Cubic (CsCl)
Lattice constant (Å)	5.43095	3.079 (a) 5.048 (c)	5.8686	5.6533	5.64613				4.2999 (a) 7.0109 (c)	6.48		4.37 (a) 12.44 (c)	3.47
Knoop hardness ($kg\,mm^{-2}$)	1150	2540	460	750	692			?	90–130	60	<10	<10	12
Melting point (°C)	1412	2827	1060	1238	958	1080	1320	1092–1295	1239	1092	408	259	460
Dielectric constant	11.7	9.7	12.4	12.8	16			10	10.2	10.9		8.8	29.8
Resistivity (Ω/cm)	$<10^{4}$	$>10^{5}$	10^{6}	10^{7}	50	10^{10}	10^{10}	3×10^{10}	10^{9}	10^{9}	10^{13}	10^{13}	10^{12}
$1/e$ abs. Depth (mm) at 10 keV	0.127	0.128	0.020	0.051	0.050	0.019	0.019	0.011	0.019	0.011	0.011	0.011	0.011
at 100 keV	23.30	17.90	1.597	3.46	3.51	1.5	1.5	1.01	1.5	1.01	0.453	0.46	0.32
Typ. FWHM ΔE (keV) at 60 keV	0.4	2.7	12	0.7	0.3	21	1.8	1.5	8.5	1.1	1.83	3.5	7.9
Intrinsic. FWHM ΔE (keV) at 60 keV (Fano noise)	0.415	0.642	0.443	0.439	0.250	0.530	0.530	0.393	0.506	0.300	0.441	0.409	0.550
Typical thickness (mm)	0.3	0.3	0.2	0.2	20	0.5	0.1	2	0.5	2	0.1	10	1

Table 1[1] Note: For comparison, the properties of the elemental semiconductors, Si and Ge, are also listed. The Fano noise was calculated using the “best” reported values of Fano factor, otherwise a value of 0.14 was assumed.

1.3 Advantages and challenges of CMT compared to other materials

Among current applied radiation detectors, CZTs are the leading devices. But the high-cost due to the limited supply of high quality, large-volume single crystals hinders their deployment. Studies have been carried to explore other applicable materials, such as CdMnTe, HgI_2 and TlBr. However, none showed vastly superior characteristics.

In the above context, CdMgTe has already shown that it possess the most desirable combination of properties needed for radiation detectors, such as high density (5.83 g/cm^3), high effective mass (49.5), high resistivity (~10^{10} Ω-cm), and high value for the $\mu\tau_e$ product (>10^{-4} cm^2/V). [11] From what is stated above, those properties are all beneficial to generating signal carriers and yielding the highest detection sensitivity.

One of the distinct advantage of CMT over CZT or CdMnTe is that the optimal energy bandgap is attainable using less Mg in CdTe. From Eq. (1), for the content of Mg of 0.1, the bandgap is 1.69 eV for the CMT material. While from Table 1, with the same composition, the bandgap is 1.572 eV for CZT, and 1.64 eV for CdMnTe.[12] It has been mentioned above that relatively large bandgap energy leads to better signal accuracy and lower leakage. Also, lower Mg concentration results in lower alloy scattering and thus increase $\mu\tau_e$. As a result, to get the same bandgap, less Mg needs be used compared to Zn or Mn. Therefore, lower concentrations of defects can be achieved.

On top of the above advantages, the segregation coefficient of Mg in CdTe is smaller than Zn in CdTe. The segregation coefficient of Mg in CdTe is reported to be aroud 1.0, while for Zn in CdTe it is 1.35. Thus, during the growth, Mg is being distributed uniformly throughout the ingot, while Zn always distributes with a relatively large concentration gradiant. As a result, CZT ingota require more zone refining, and have more compositional defects in the crystal. Fig. 1.1 illustrates the segregation coefficients of different metals in CdTe.

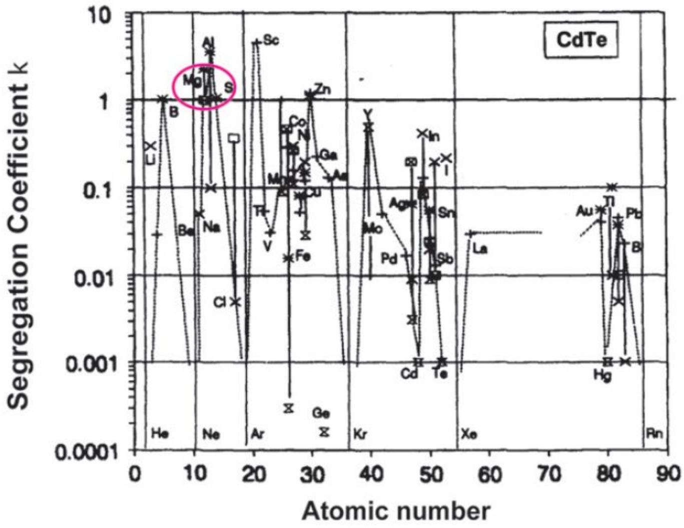

Fig. 1.1 Segregation coefficients of various matals in CdTe. [11]

Mn has similar segregation coefficient in CdTe as Mg and it also has bandgap advantage compared to CZT, so CdMnTe is also among the few novel materials to show spectroscopic results at X-ray wavelengths. [1] But the bonds ionicity of CdMnTe is a problem. The ionicty of bonds in CdMnTe is slightly higher than that in CZT, so, although CdMnTe grows in the zinc blende structure, it is possible that it contains hexagonal inclusions. Moreover, higher tendency of twining has been observed in CdMnTe. [12]

$CdTe_{1-x}Se_x$ has been regarded as an another alternative material for gamma ray detectors. [13] This material can form the zinc blende structure up to $x = 0.2$ and shows no separation beteween the solidus and liquidus of CdTe-CdSe pseudo-binary phase diagram, that ensure homogeneous material. However, when x reaches 0.2, the bandgap reduces and goes below the energy bandgap of CdTe. The latter results in larger leakage current. Another factor that hinders CdTeSe applications is the limited purity for commercially available selenium and the resulting high cost of the high quality detector material.

Another important advantage of CMT concerns with the lattice constant. The similar lattice constant of CdTe and MgTe ensure good crystallinity of CMT. Also the lattice parameters ratio of MgTe shows zinc blende structure. So it is easier for Mg to fill in the CMT crystal structure and form high quality single crystals. These factors ensure fabrication of large-volume defect-free single crystals, that should, ultimately, reduce the production cost of large-area devices. Fig. 1.2 shows the relationship between energy bandgap and lattice constant of various alloys.

An interesting property worth to be mentioned is that the Mg ions are mobile to some extent, so they can occupy some of the Cd vacancies because of their light mass and small radius compared to Cd and Te atoms. This is beneficial to the crystal quality as well. [11]

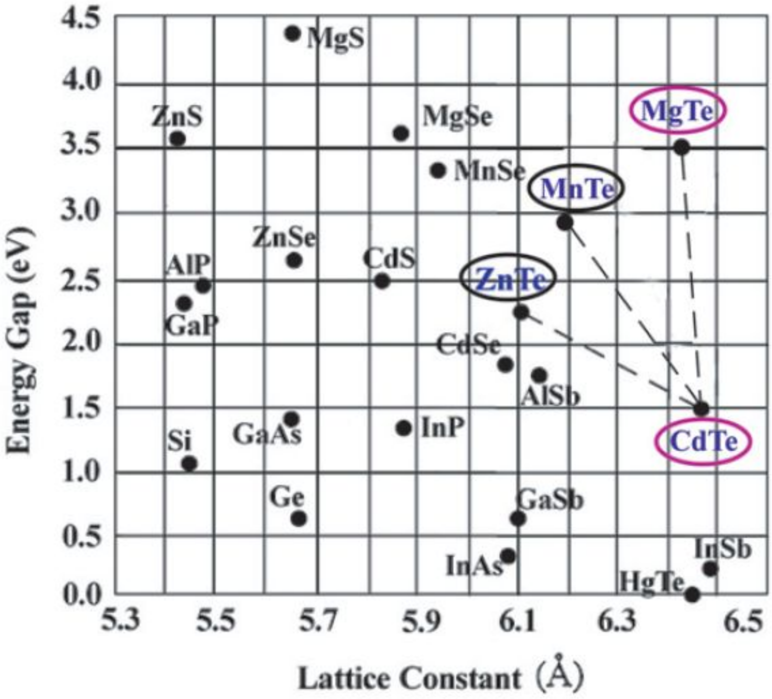

Fig. 1.2 Lattice constant and dependence of energy bandgap of various alloys. [11]

With so many advantages, CMT is the most promising material for radiation detectors. Unfortunately, some papers illustrate the explosion concern during fabrication [11], however, fabrication of CdZnTe also suffers from the same problem. Since the reaction is exothermal, it can be dangerous if the reaction conditions are not controlled properly. Extreme care needs to be taken when achieving a thorough mixture of the melt in order to avoid the rupture of the ampoule due to superheating of the elemental constituent. Finally, researchers need to select proper crucible materials that would not cause too much adherence on the crucible walls.

1.4 Applications and motivations

Besides the expected application in radiation detection, CMT has been reported to be implemented in other research areas. Many papers present fabrication of heterostructures based on CMT, and most of them are quantum wells. It is popular, because of the CMT tunable energy bandgap, and it is always in conjunction with CdTe-based quantum wells. The CMT layers form the wells and CdTe forms the barriers. Q. X. Zhao and M. Oestreich presented magneto-optic investigation of single CdTe/CdMgTe quantum wells by stationary and time-resolved photoluminescence. [14] They studied the dependence of the electron and hole g factors and found the electron spin phase relaxation time much shorter than the GaAs/AlGaAs system.

CMT is also reported to be fabricated into tandem solar cells, and usually being used as the top cell. Tandem solar cells typically have two parts, the top-cell and the bottom-cell, and top cells use materials with larger bandgap so they absorb high energy photons, while transmitting lower energy photons later absorbed by the bottom cell. By this means, the spectrum gets split and the use of a solar cell is optimized to each section of the spectrum. L.A. Kosyachenko and his group fabricated a two-terminal tandem solar cell with the structure of CdMgTe/Cu(In,Ga)Se_2, which took advantages of the proper bandgap of CMT. [16] The same group also formed many other tandem solar cells by using CMT. [17,18]

For any photoelectronic application, it is quite important to understand optical photoresponse and its dynamics in CMT and what are the main relaxation channels of photoexcited carriers. The latter is also crucial for understanding the physics of the photoconductive effect in CMT for radiation detector applications. In this thesis, we present our studies on the ultrafast photoresponse and nonequilibrium carrier dynamics in CMT using femtosecond pump-probe spectroscopy. Next, we modeled our measured waveforms to get detail information of the carrier dynamics on a picosecond time scale.

Chapter 2: Experimental Techniques

2.1 Mode-locked femtosecond laser system

The laser used in our experiments is a self-modelocked femtosecond Ti:sapphiere oscillator (MIRA) fabricated by Coherent, which is one of the most commonly used commercial femtosecond-pulse lasers. The Ti:sapphire laser generates pulses with an average optical power of 1.6 W when pumped by a 10 W continuous green wave (532 nm), using a VERDI laser. The MIRA output features 100-fs-wide pulse and a very broadly tunable wavelength spectrum ranging from 600 nm to about 1050 nm. Such wide emitting spectrum results from band splitting due to distortion in the lattice by Ti^{3+} substitution of Al^{3+} in the sapphire lattice. [19] Fig. 2.1 shows the absorption and emission spectra for Ti:sapphire. The broad absorption spectrum and the fluorescence spectrum allow for a multitude of pumping lasers to be used with this crystal, which makes it best suited for creation of femtosecond pulses.

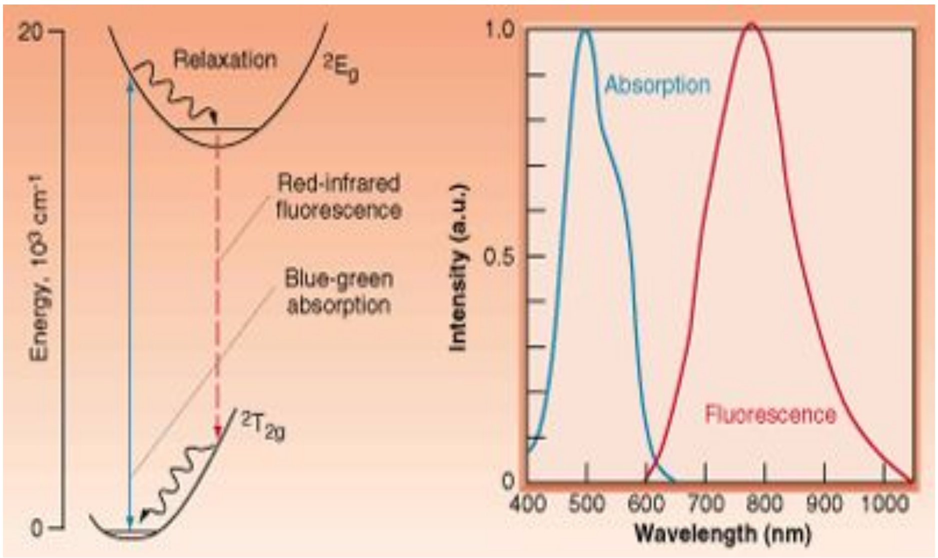

Fig. 2.1 The energy band diagram (left), and the absorption and emission spectra of Ti:Sapphire. The interaction of Ti^{3+} and the Al_2O_3 lattice makes wide-spreading energy level, and thus broad tuning.

The mode-locked pulses are achieved by the optical cavity. The light reflects between the mirrors and interfere constructively and destructively with itself, leading to the formation of standing waves or modes between the mirrors. If the length of the laser cavity is L, the frequency difference between two adjacent modes is $c/2L$, where c is the speed of light. Lock-in phases create a constructive interference pattern between the modes, resulting in a pulsed light emission. The final pulse width is determined by the amount of modes that are locked [20].

Mode-locking is achieved by a nonlinear optical effect, called the Kerr effect. Basically, it refers to a change in the refractive index of a material in response to an applied electric field. Larger intensity of light leads to a higher refractive index under the Kerr effect. Following the intensity distribution of the laser beam, the center of the beam travels under higher refractive index than the peripheral area, thus the center of the beam propagates slower, effectively creating a lensing effect. Since the intensity of the continuous wave (CW) mode is lower than the peak intensity of a pulsed beam, the CW mode is less focused. Using a slit to block the outer region of the beam, so that the CW mode is blocked, resulting in a self-amplifying pulsed beam, as shown in Fig. 2.2 [20, 21]

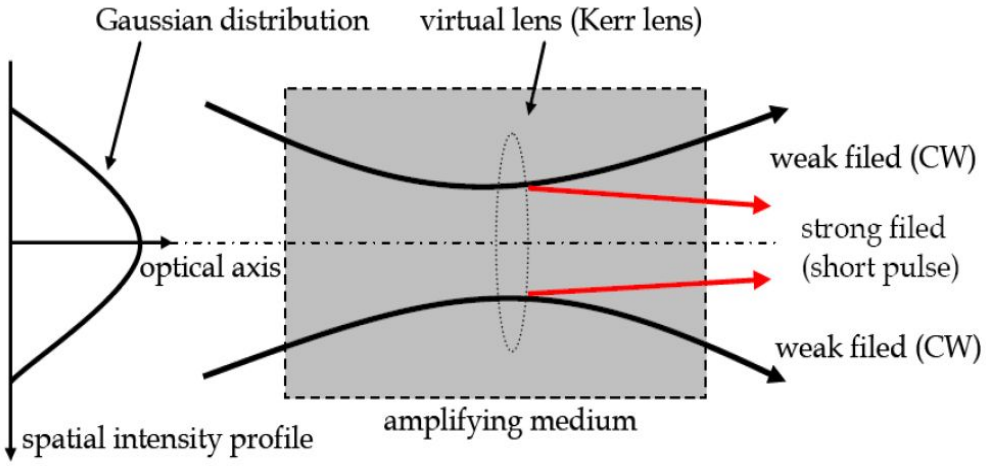

Fig. 2.2 Self-focusing of Kerr lense effect, the outer region of the CW beam is then blocked away by a slit, resulting a self-amplifying pulsed beam.

2.2 Pump-probe spectroscopy

Femtosecond pump-probe spectroscopy is a very useful tool for investigation of ultrafast (sub-picosecond to a few nanoseconds) nonequilibrium carrier dynamics in condensed matter materials. In a pump-probe technique, an ultrashort laser pulse is separated into two pulses, the pump pulse and the probe pulse, and the probe pulse is delay variably with respect to the pump pulse. The two beams focus on the same spot of the tested material. Usually the probe beam spot should be located completely within the pump beam spot. The intensity of the pump beam is much larger than that of the probe beam (usually more than 10 times). In equilibrium, energy exchanges though the carrier-carrier or carrier-phonon interaction result in carrier and phonon energies being distributed uniformly so the material keeps a common temperature.

Fig. 2.3 depicts the basic processes a semiconductor goes through after it gets excited by light that of energy greater than the bandgap [23,24]. Upon absorption [Fig. 2.3(a)], excited electrons and holes will possess narrow energy distributions and peak in particular directions of momentum space under the excitation of a monochromatic and polarized radiation. Within tens of femtoseconds, carrier-carrier scattering events randomize the carrier momentum and make the carriers form the Fermi-Dirac distribution. [Fig. 2.3(b)]. Since electrons have much smaller effective mass than holes, the electrons will possess most of the excess kinetic energy. Therefore, it is reasonable to consider electrons and holes under different thermal distributions. The distribution functions for electrons and holes have different effective temperatures that maybe higher or lower than the lattice equilibrium temperature. As time evolves, the electrons lose their excess kinetic energy via various scattering mechanism, the most efficient mechanism is optical-phonon and, subsequently, acoustic-phonon scattering. [Fig. 2.3(c)] When the electrons and holes have settled to the bottom of the conduction band and top of the valence band respectively, they recombine finally either radiatively or nonradiatively. [Fig. 2.3(d)] [25, 26].

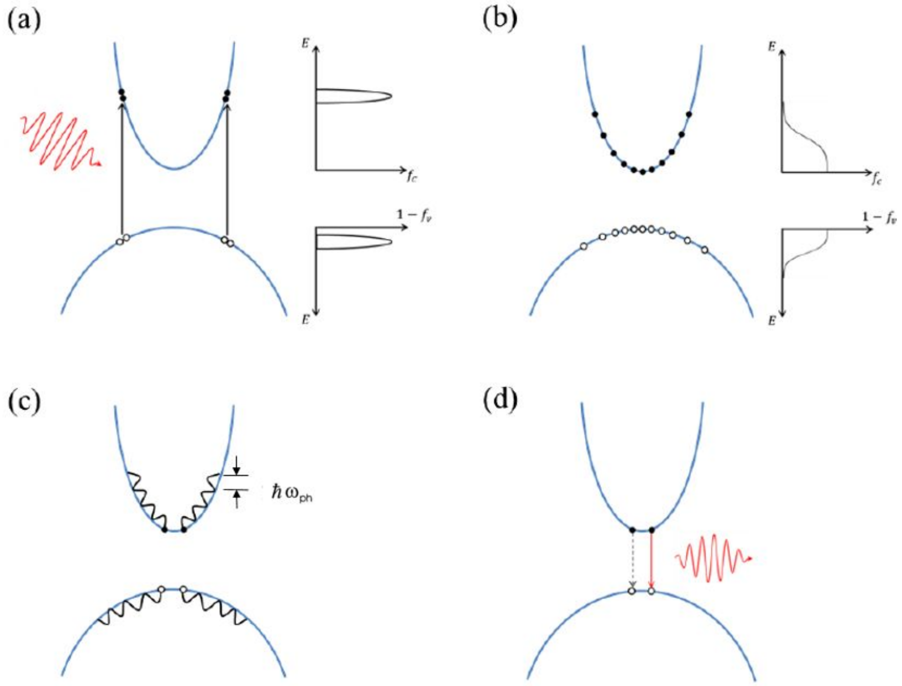

Fig. 2.3 The photoexcitation of a semiconductor and subsequent energy relaxation. (a) Right after excitation, the carriers will have delta function distribution in energy and momentum space. (b) Electrons and holes thermalize into separate Fermi-Dirac distributions. (c) The carriers lose their excess kinetic energy through various scattering mechanism while approaching thermal equilibrium with the lattice. (d) Electron- hole radiative (red arrow) and non-radiative (black dotted line arrow). Adapted from [23]

In pump-probe spectroscopy, the pump beam is used to create perturbation and cause change of optical property, e.g., sample reflectivity. The low intensity probe beam is used to measure the resulting change in, e.g. change of the index of refraction. The probe beam goes through a precisely varied path length that allows for femtosecond resolution of the time delay between two beams. When the path length of the probe beam is shorter than the pump beam, the probe pulse will arrive the sample first (before the photoexcitation). In this case, the probe beam will measure the reflectivity of the sample in equilibrium (no pump excitation). When the path length of the probe beam equals to that of the pump beam, both beams arrive the sample at the same time. Thus, the probe beam will measure the reflectivity change when the material gets excited. As the path length of the probe beam gets longer and longer, the nonequilibrium relaxation process is measured. Fig. 2.4 shows an example pump-probe measurement with the events labeled.

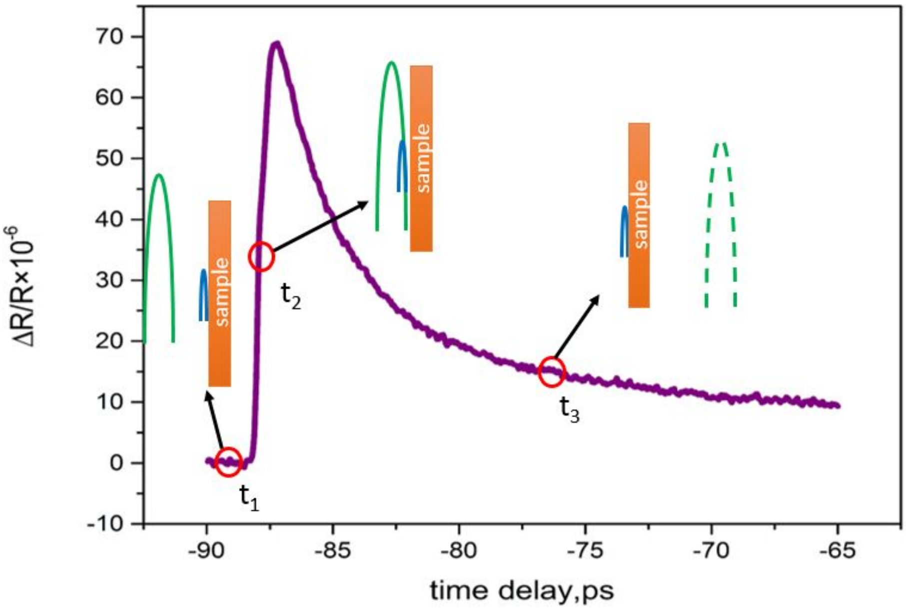

Fig. 2.4 An example of pump-probe measurement. At t_1, the probe pulse (blue pulse) arrives at the sample before the pump pulse (green pulse) and measures the equilibrium state of the sample. At t_2, the pump and probe pulses arrive the sample simultaneously and the sample is measured at mid-excitation. After the excitation of the pump beam, the carrier relaxation dynamics are measured at t_3.

The pump-probe signal can be absorption, phase shift, birefringence or diffraction of the probe pulse itself, or generation of fluorescence, photoelectrons or ion induced by the probe photon. [25]

2.3 The pump-probe experimental setup

Figure 2.5 shows the schematic picture of our pump-probe setup. The laser system used for experimentation in this thesis is a commercial MIRA 900 mode-locked

Ti:Al_2O_3 laser produced by the company Coherent [26]. Mira 900 is pumped by a commercial Neodymium Vanadate laser also produced by Coherent and called Verdi V10 [27]. Mira is tuned to produce 800 nm wavelength laser pulses with duration of about 100 fs and repetition rate of 76 MHz [26]. After the output from Mira, the laser beam is separated by a beamsplitter which directs ~60% of the intensity to the pump path, and ~40% of the intensity to the probe path. In order to prevent pump beam being detected and create an artifact signal in a single-color pump-probe measurement, one polarizer and a half-wave plate are set on the path of the pump beam. The polarizer is adjusted so that most of the laser energy can get though with the same polarization, then half-wave plate turns the polarization to be orthogonal to the original polarization. Another polarizer is set on the path of the probe beam with the same polarization with the output beam (orthogonal to the pump beam). Therefore, the two beams are of orthogonal polarization, what ensures their separation in the detection part of the system.

The pump beam is modulated by an acousto-optic modulator at ~100 kHz. The beam is attenuated (if needed) through a series of neutral density filters and focused onto the sample with a spot diameter of about 45 μm at a 68° incidence angle with respect to the sample normal. The probe beam path length is changeable by using a translational stage with a retroreflector to vary the time delay between the pump and probe pulses. The probe beam is attenuated by a series of neutral density filters and focused onto the sample at normal incidence with a spot size of ~15 μm. It arrives at the sample plane and is reflected back. Next, it passes through another polarizer which is of the same polarization as the initial one to make sure that pump/probe beams are crossed-polarized and only the reflected probe light reaches the photodetector. The photodetector senses the light and translates it into an electronic signal, that is next separated into AC and DC components by a bias-Tee. Then the DC component is measured by a voltmeter and AC component by a lock-in amplifier (LIA). The two signal components are necessary to measure the normalized change in reflection $\Delta R / R$.

LIA can detect and measure very small signals (down to the nanovolt scale) over noise that is thousands of times larger. It also provides a reference frequency to the acousto-optic modulator in the pump beam path. When the pump beam and probe beam reach the sample, the reflection of probe beam will be altered at the pump beam modulation frequency causing the probe beam signal to vary at that frequency. The LIA works as frequency filter and measures the signal value at a given time delay between the pump and probe pulses. [28]

When pump-probe measurement is proceeding, the translation stage moves step by step according to the resolution that been set, altering the time difference when the pump and probe pulses arrive at the sample. The translational stage is capable of micrometer precision, so it can easily get sub-50 fs resolution. The LIA records the signal at each point of the delay line, and the total transient waveform is recorded by a computer.

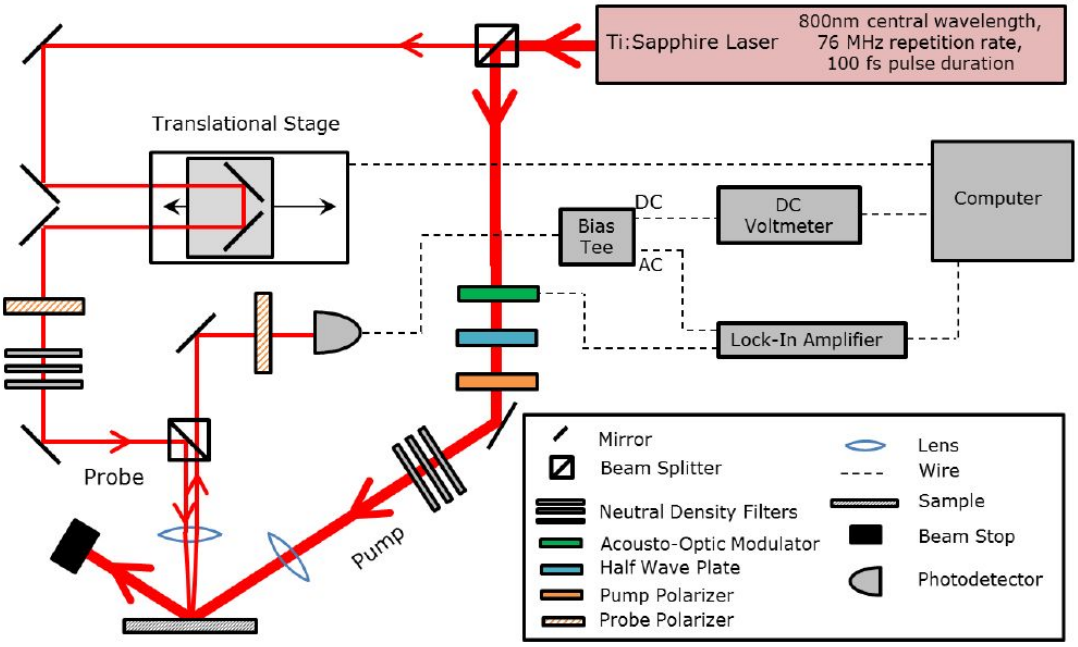

Fig. 2.5 Simplified setup for degenerate (single-color) pump-probe spectroscopy measurements.

2.4 Sample fabrication

The semi-insulating CMT samples used in our experiments were fabricated by Brookhaven National Laboratory (NY 11973, USA). The specific samples we test comes from the batch called B8. Its composition is $Cd_{0.92}Mg_{0.08}Te$, and the material is doped by indium in order to reduce the defects, and increase resistivity of the material. Its bandgap is ~1.61 eV, and resistivity is ~10^9 Ω·cm. The sample is an “as-grown material”, i.e., there was no post-grow heat treatment such as annealing. The sample was grown by the high-pressure Bridgeman (HPB) technique with a vertical three-heat zone tubular furnace. This method has been maturely developed for CdZnTe, and CdMnTe [29].

So in order to get the CMT ingots with high quality, i.e., with low defects and homogeneous stoichiometry, three steps need to be taken: compounding, Bridgman technique, and zone-melting refining. Raw CMT compound is made by melting Cd, Mg, and Te, and reacting to form a ternary compound. Fig 2.6(a) shows a schematic diagram of an HPB furnace. The conventional Bridgman furnace houses inside a high-pressure chamber, since the melt consists of volatile components, and the constituents would dissipate to the vapor phase above the melt. Since Cd has the highest vapor pressure, the vapor phase predominantly consists of Cd atoms (Fig. 2.6(b)).

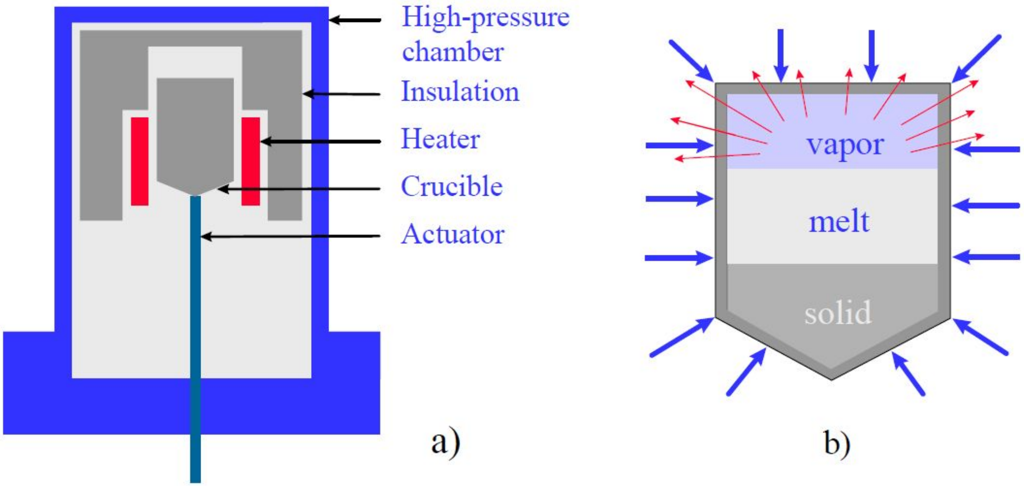

Fig. 2.6 Schematic diagram of HPB furnace (a), and the principle of HPB growth (b). [29]

Chapter 3:Results and Discussion

3.1 Pump-probe measurements

For a probe beam with very low intensity (so small that it would not affect the influence of pump beam), the refractive index change Δn of the tested material, induced by the pump-induced photoexcited electron density N can be described by the simple Drude model, which expresses Δn as

$$\frac{\Delta n}{n} = -\frac{2\pi e^2}{\varepsilon_0 \varepsilon_b \omega^2} \cdot \frac{N}{m^*}, \tag{2.1}$$

where n is the refractive index of the sample, $\varepsilon_0 \varepsilon_b$ is the background dielectric function at low frequencies, e is the unit electronic charge, ω is the probe angular frequency, and m^* is the effective electron mass in the conduction band, respectively. The contribution of holes to Δn is neglected, because holes typically have a much heavier effective mass than electrons. Equation (2.1) shows that Δn changes linearly with the density N of the conduction-band electrons [30,31].

For pump-probe spectroscopy measuring the reflection signal, the probe beam differential reflectivity $\frac{\Delta R}{R}$ is defined as

$$\frac{\Delta R}{R} = \frac{R' - R}{R}, \tag{2.2}$$

where R' and R are the probe beam reflectivities in the presence and absence of the pump beam, respectively. For thick samples, as in our case, R at normal incidence is defined as

$$R = \left(\frac{n-1}{n+1} \right)^2. \tag{2.3}$$

Since R depends only on n, the normalized change in the reflectivity $\Delta R / R$ can be written as

$$\Delta R / R = \frac{d(\ln R)}{dn \Delta n}. \tag{2.4}$$

Substituting Eq. (2.1) into the above equation, the relationship between $\Delta R / R$ and N can be expressed as

$$\Delta R/R = -\frac{2\pi n e^2}{\varepsilon_0 \omega^2}\frac{d(\ln R)}{dn}\frac{N}{m^*}. \tag{2.5}$$

Eq. (2.5) clearly shows that $\Delta R/R$ varies linearly with N. Therefore, the time-resolved, experimental $\Delta R/R$ signal gives us directly the time evolution of photo-excited electrons in the conduction band.

Another problem is the relationship between the intensity of the pump beam and the electron number in the conduction band. Because we want to make sure the $\Delta R/R$ signal reflects precisely how the electron concentration changes. So by changing the attenuation filters set on the pump path, the intensity of pump beam can be varied. By taking $\Delta R/R$ measurements under different pump beam power densities, a series of photoresponse curves are recorded and presented in Fig. 3.1.

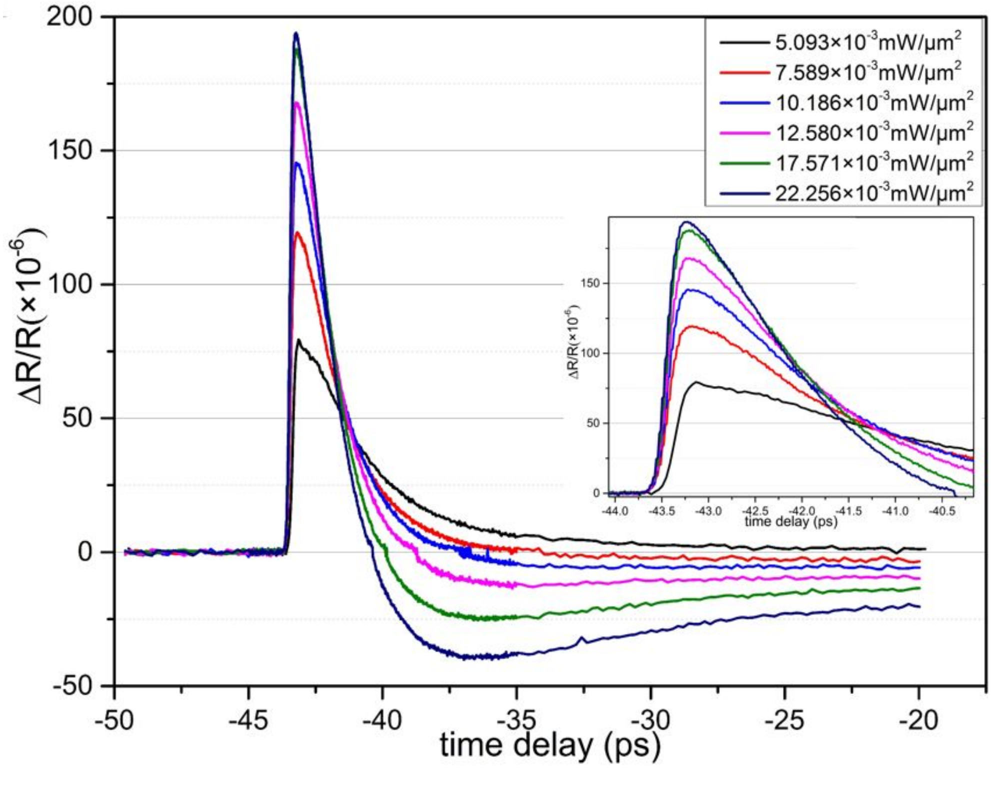

Fig. 3.1 Pump-probe measurements of CMT sample with different pump beam power density (see legend). The inset shows the peak area of the measurements.

Fig. 3.1 shows that in each case the signal reaches a sharp peak right after the CMT sample got illuminated, and then relaxes back to equilibrium. The latter follows relaxation mechanisms discussed in section 2.2. Interestingly, for large pump beam powers, the $\Delta R / R$ signal becomes negative at the later stage of relaxation. The signal also gets larger as the increase of the pump beam intensity. Fig. 3.2 shows the dependence of the signal magnitude on the pump beam power intensity.

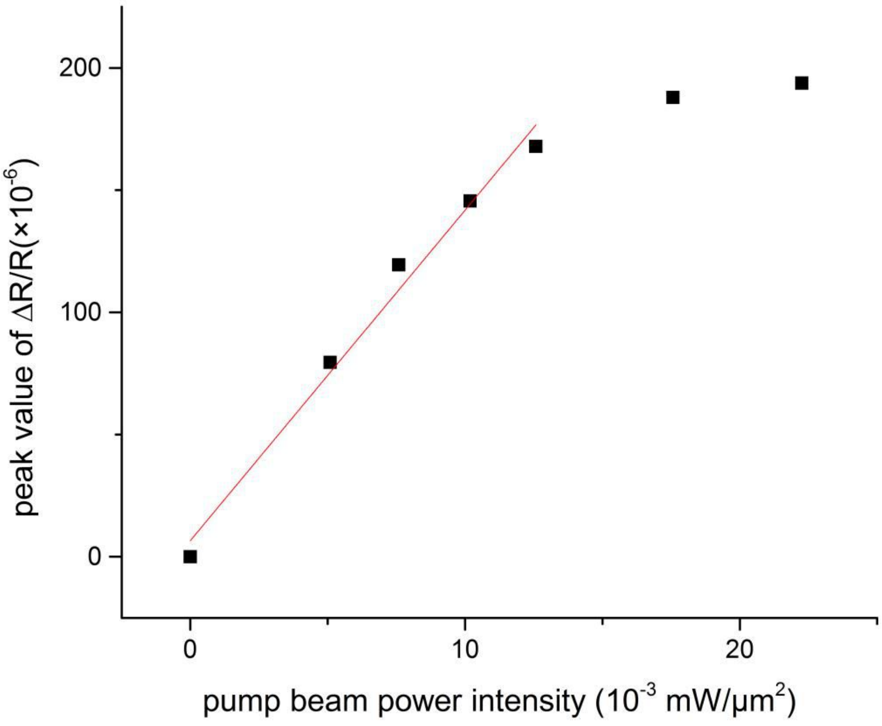

Fig. 3.2 Peak values of $\Delta R / R$ varies as pump beam power density

Fig. 3.2 shows that when we are in the low intensity regime, the signal magnitude increases linearly with the pump beam power, but as the pump gets larger and larger, the signal deviates from the linear dependence and reaches saturation. The saturation is related to the simple heating effect of the sample by the very intense pump. Therefore, in order to make sure the signal collected reflects the the states of electrons precisely, the pump beam power has been controlled within the linear region for all our measurements.

3.2 Transient photoresponse dynamic model construction of CMT sample

Jepsen *et al.* [32] have implemented a dynamical model that involves shallow trap sites in the band gap to reproduce the transient photo response of carriers in optically excited and THz-probed microcrystalline Si wafers. Conceptually, a very similar model was earlier used for the analysis of femtosecond optical pump-probe studies of the transient photoresponse dynamics in low-temperature-grown GaAs films [33]. Their model prove very large concentration of traps due to a distorted lattice and as precipitates. Here, we derive a general model that contains all the scattering mechanisms for a CMT sample that are reasonable for the 800-800 nm pump-probe measurements and then we adjust the model based on our experimental data. We note that our general model includes both [32] and [33] approaches.

Section 2.2 in chapter 2 has described general excitation and relaxation processes of photo-excited electrons. Here we introduce a more detailed model for CMT sample, as shown in Fig3.3. Since as grown sample has a very high resistivity, traps should be included. So in-gap trap states are presumed, and there might be electrons trapped in there in equilibrium. Also, besides the normal pumping process that excites electrons up to the conduction band ($I\alpha$ in Fig. 3.3), we include the two-photon-absorption process (the TPA $I^2\beta$ process in Fig. 3.3), which indicates that some electrons might simultaneously absorb two photons and reach higher energy states, and, thus, becoming hot electrons. Another process that we include is the fact that trapped electrons can also absorb photons and be promoted to the higher energy state ($I\gamma$ part in Fig. 3.3). During the relaxation hot electrons can cool down by losing their energy through an electron-optic-phonon interaction, gradually dropping towards the bottom of the conduction band, or even be re-excited back by phonon absorption to hot states (the processes indicted with two narrows labeled τ_{cool}). Finally, electrons at the bottom of conduction band can either get trapped or recombine with holes. Another option for hot electrons is immediate trapping by intra-band states ($\tau_{trap,hot}$).

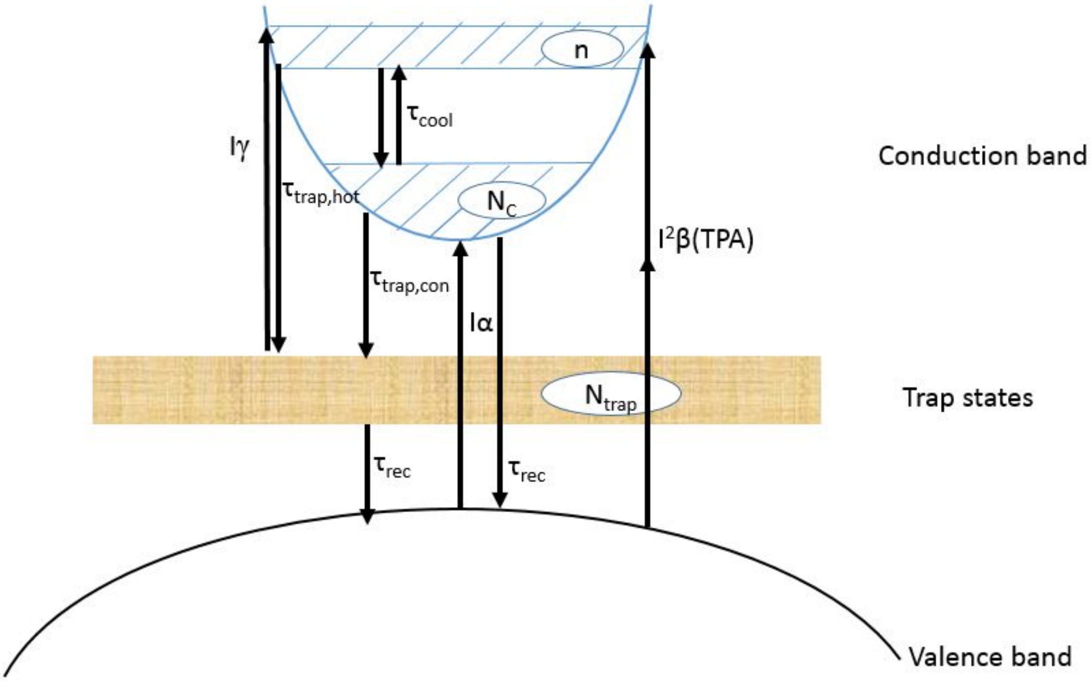

Fig. 3.3 Schematic band diagram with presumed dynamic processes.

Fig. 3.4 provides a simplified graph that schematically includes all the processes discussed above. In future discussions, we will only use this kind of graph. Based on the processes presented in Fig. 3.4, we describe the time dynamics of the carriers in CMT by the following set of differential equations:

$$\frac{dN_C}{dt}=\frac{I\alpha}{h\nu}+\frac{n}{\tau_{cool}}-\frac{N_C}{\tau_{trap,con}}-\frac{N_C}{\tau_{cool}}-\frac{N_C}{\tau_{rec}} \tag{3.1}$$

$$\frac{dn}{dt}=\left(\frac{I}{h\nu}\right)^2\beta+\frac{I}{h\nu}\gamma+\frac{N_C}{\tau_{cool}}-\frac{n}{\tau_{cool}}-\frac{n}{\tau_{trap,hot}} \tag{3.2}$$

$$\frac{dN_{trap}}{dt}=-\frac{I}{h\nu}\gamma+\frac{N_C}{\tau_{trap,con}}+\frac{n}{\tau_{trap,hot}}-\frac{N_{trap}}{\tau_{rec}} \tag{3.3}$$

where N_C is the concentration of electrons in the bottom of the conduction band; I is the pump beam intensity with photon energy $h\nu$; α is the band-to-band absorption coefficient; τ_{cool} is the cooling time when electrons relax from the hot state to the bottom of the conduction band; $\tau_{trap,con}$ is the trap time of electrons initially at the bottom of the conduction band; $\tau_{trap,hot}$ is the trap time of electrons in the hot state, τ_{rec} is the electron-hole recombination time; n is the concentration of hot electrons; β is the TPA coefficient; γ is the trap-to-hot pumping coefficient; $\tau_{trap,hot}$ is the trap time of hot electrons; N_{trap} is the concentration of trapped electrons.

Eq. (3.1) is the change of electron concentration at the bottom of the conduction band, while Eq. (3.2) is the change of photoexcited, hot-electron concentration. Finally, Eq. (3.3) describes the change of trapped-electron concentration. The first term on the right side of Eq.(3.3) is negative because the pumping of trapped electrons depopulate the trap sites.

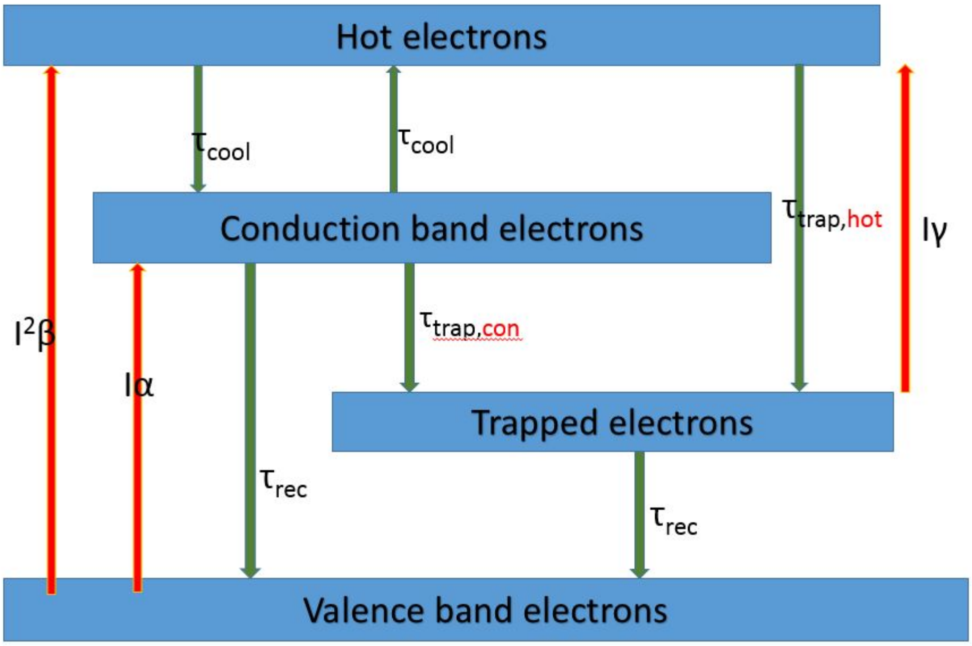

Fig. 3.4 Schematic graph of presumed ultra-fast dynamic processes

The generation rate of electrons is given by the Guassian optical pulse, $I(t) = I_0 \exp(-4\ln 2\frac{t^2}{\tau_p^2})$ with FWHM of $\tau_p = 100\,\text{ps}$. Following, Eq. (2.5), our experimentaly measured $\Delta R/R$ signal is directly proportional to the total $N(t)$. Thus, $N(t)$ can be derived as

$$N(t) = N_C(t) + n(t) - N_{trap}(t)\,, \tag{3.4}$$

where $N_C(t)$, $n(t)$, and $N_{trap}(t)$ are the solutions of our starting differential equations (3.1) - (3.3). Note that the sign in front of N_{trap} is negative, since traps lower the concentration of excited carriers.

For our data analysis, we chose a group of signals [see Fig. 3.5(a)] corresponding to the pump beam power is in the linear region, and normalize their peak amplitude to 1. Next, we use the software Matlab to smooth the signal, and finally, fit them with the solution of the set of differential equations, (3.1) - (3.3). Fig. 3.5(b) shows a particular experimental waveform, the signal with the pump beam power as 30.8mW.

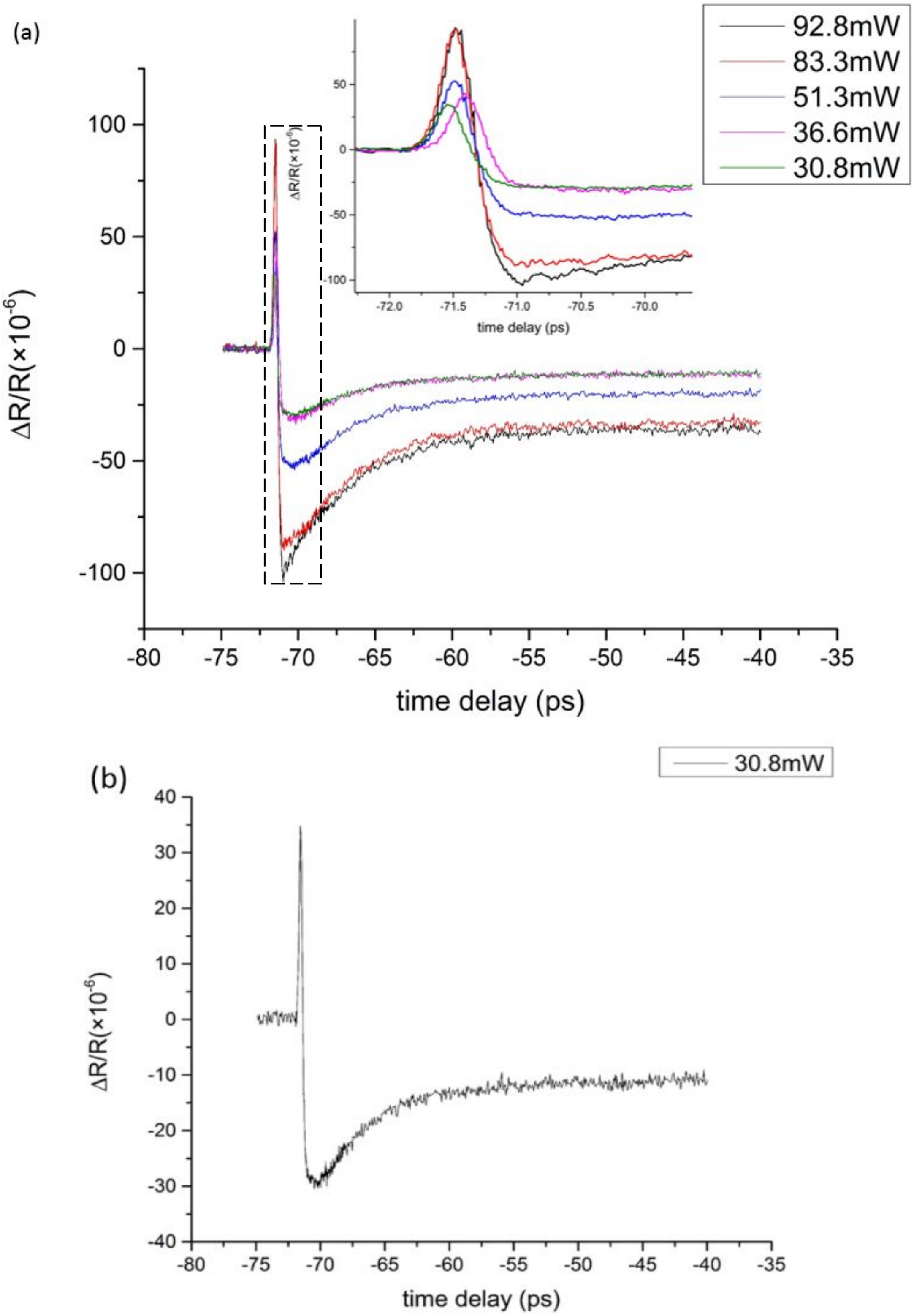

Fig. 3.5 The group of data used for simulationss (a), the inset shows the pumping part, and one of the signal with pump beam power as 30.8mW. (b)

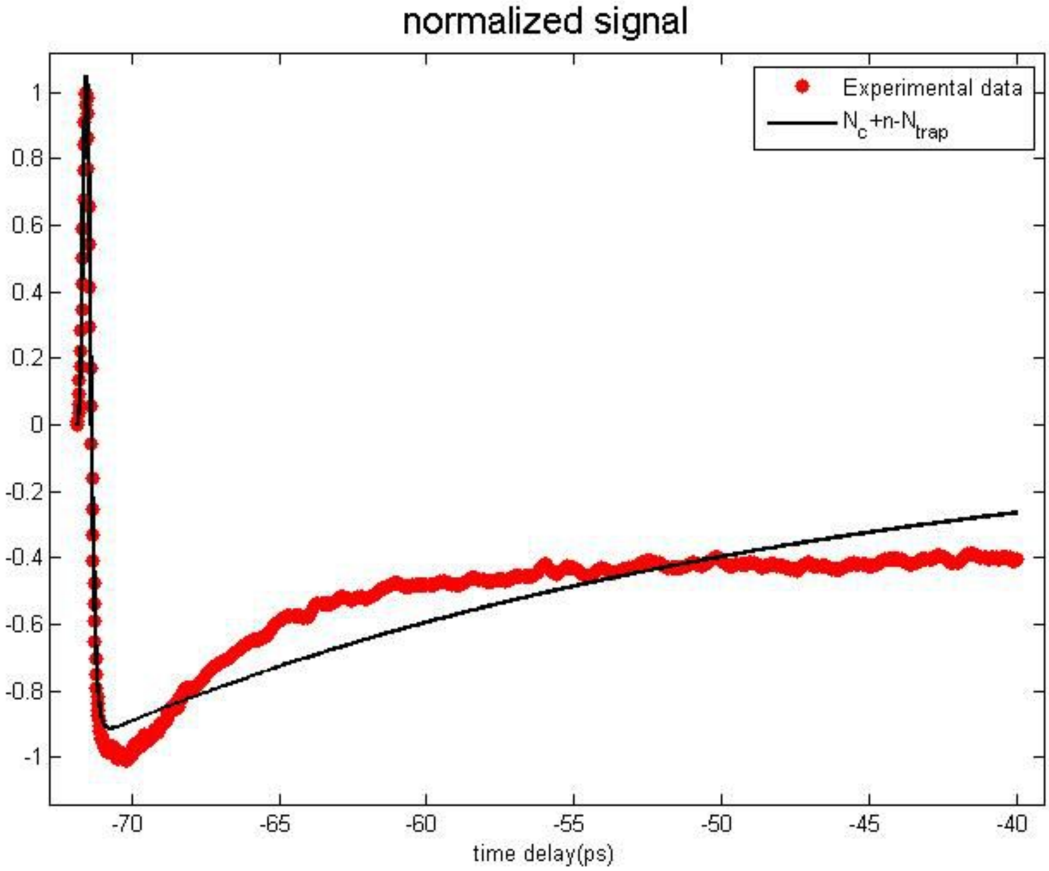

Fig. 3.6 The simulation result (red dots) for experimental data with pump beam power of 30.8 mW (black line).

Fig. 3.6 presents the same experimental data as Fig. 3.5(b), but now we also include our first fitting attempt. The change of N_C and n is faster than N_{trap}, and the tail of the signal is dominated by N_{trap}. But the tail of the signal is not tilted well, since the experimental data drop faster than the simulation result and then reach the saturation. The process that can affect the tail is the recombination process. So we try to vary τ_{rec} to be larger to see the change and the result is shown in Fig. 3.7.

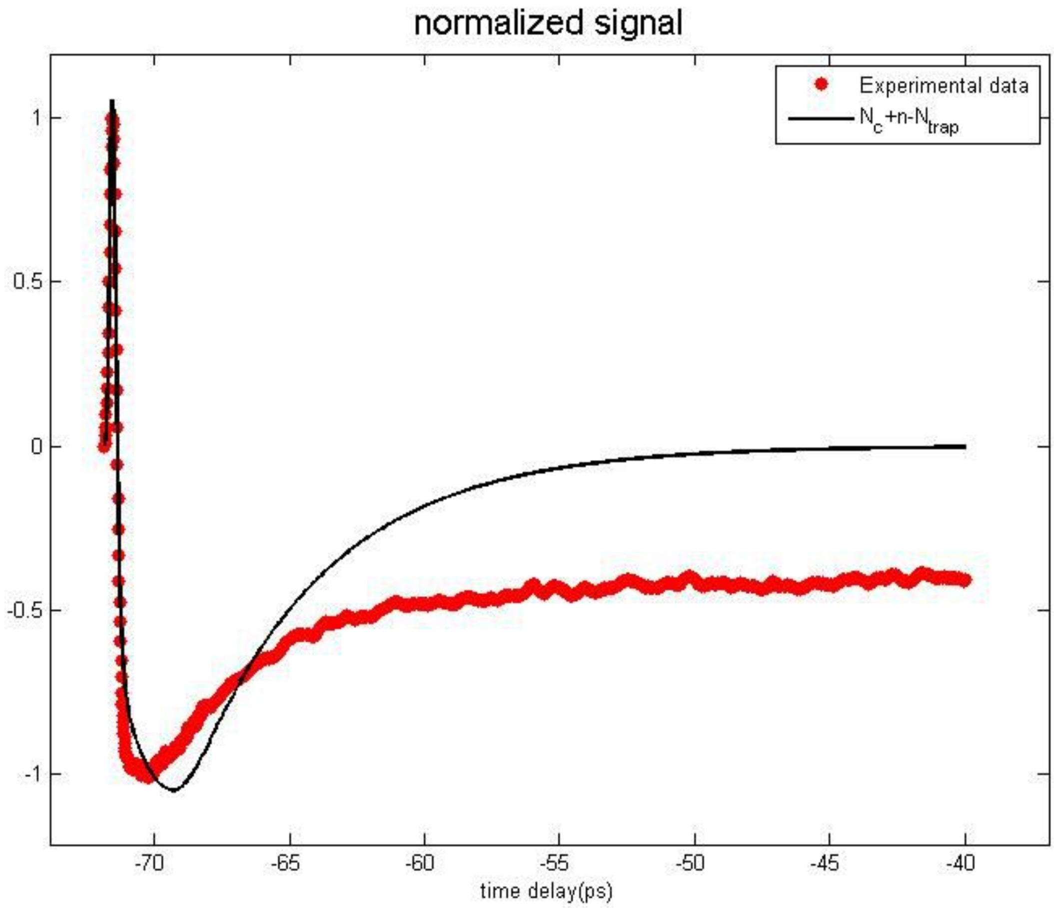

Fig. 3.7 The experimental data (red dots) and simulation result (black line) with shorter τ_{rec}.

From Fig. 3.7 we find out that during the first ~20 ps after pumping, concentration of trapped electrons decreases fast but then the decrease slows down. The experimental signal does not return to zero within our time window, suggesting that some electrons are trapped “forever”. At the same time, our simulations always try to make N_{trap} return to zero finally. Thus, we need to add one more parameter which would correspond to the concentration of electrons trapped forever $N_{trap,final}$. Thus, the number of electrons which can recombine with holes should be $N_{trap} - N_{trap,final}$. Therefore, Eq. (3.3) becomes

$$\frac{dN_{trap}}{dt} = -\frac{I}{h\nu}\gamma + \frac{N_C}{\tau_{trap,con}} + \frac{n}{\tau_{trap,hot}} - \frac{N_{trap} - N_{trap,final}}{\tau_{rec}} \tag{3.4}$$

Next, we simulate the same experimental data again and Fig. 3.8(a) shows that the fit is almost perfect. Table 3.1 shows the simulation parameters, while Fig. 3.8(b) presents numerical solutions of $N_C(t)$, $n(t)$ and $N_{trap}(t)$.

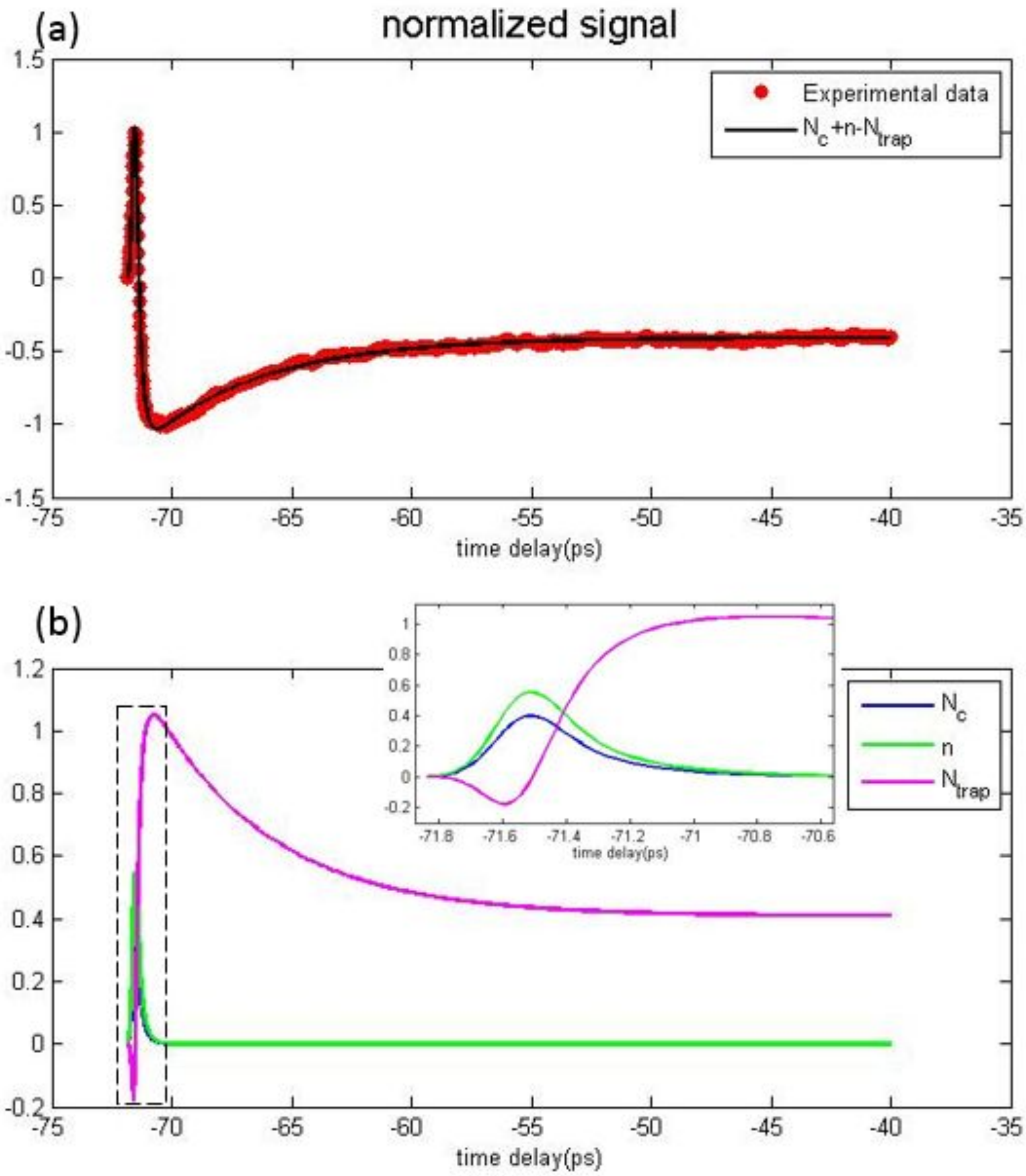

Fig. 3.8 (a) Simulation result (black line) with final trapped electrons considered for experimental data with pump beam power of 30.8 mW (red dots). (b) Corresponding numerical solutions of $N_C(t)$, $n(t)$ and $N_{trap}(t)$. The inset shows the pumping part.

Table 3.1 The simulation parameters of the experimental data with pump beam power of 30.8mW.

$\frac{I}{h\nu}\alpha$	$\left(\frac{I}{h\nu}\right)^2\beta$	$\frac{I}{h\nu}\gamma$	τ_{cool} (ps)	$\tau_{trap,hot}$ (ps)	$\tau_{trap,con}$ (ps)	τ_{rec} (ps)
4.93	0.001	4.39	84.44	0.122	0.127	5.12

From Fig. 3.8(b) we can see that right after the excitation, $N_{trap}(t)$ dips down into negative part and then immediately goes back and increases dramatically. The initial dip indicates that traps have been filled before excitation and when the sample got excited, some of the trapped electrons absorbed photons and got transfered to the conduction band (the process labeled $I\gamma$ in Fig. 3.4). From Table 3.1, $\tau_{trap,hot}$ and $\tau_{trap,con}$ are extremely short compared to other processes, what means that after electrons get pumped up to the conduction band, they get trapped, essentially, immediately. Also, these two parameters are quite close to each other, so we are going to make them equal and set them to be τ_{trap}. We noticed that τ_{cool} is much longer than other processes. Since $1/\tau_{cool}$ indicates the probability of electron-phonon scattering, it means that this relaxation channel is much less probable as compared to other processes. This fit also proves that some electrons got trapped for a long time and cannot recombine with holes. Finally, we note that during the excitation, conduction band and hot-electron states got almost equally populated ($N_{hot} \geq N_{con}$) and very quickly relax down transfering electrons to traps.

3.3 Adjustments of the dynamic model and dynamic analysis

After the construction of our basic simulation, we have quite good understanding of for the dynamic processes of photoexcited electrons in CMT. Now we try to make our model more precise. In our earlier simulations, we set the carrier trap-time to be constant, which indicates that we assume there exist so many traps in the material that those traps cannot be all filled, i.e., the number of traps is much larger than the number of excited carriers. But this assumption may not accurate at least for high-intensity excitations and it is more reasonable to assume that there is a limited number of traps and when the number of trapped electrons increases, less traps remain available, and it takes longer for electrons to find a "place" to go. Therefore we assume that τ_{trap} is, as in [32], a function of the number of available trap sites and their individual lifetimes, and is given by

$$\tau_{trap} = \frac{\tau_{trap,\min}}{1 - \dfrac{N_{trap}}{N_{trap,\max}}} \tag{3.5}$$

with the $N_{trap,\max}$ and $\tau_{trap,\min}$ representing the maximum concentration of trap sites in the sample and shortest trapping time, respectively. Another thing we noticed in former simulation result is that in Table 3.1, $I^2\beta$ is much smaller than $I\alpha$ or $I\gamma$. It always reaches the lower-bound set in the Matlab program (Appendix 2.2), it means that two-photon-absorption is almost negligible, at least for the measurement with the pump beam power of 30.8 mW. But we still keep this term to check if it could become more pronounced when the larger pump beam power is used.

So now we adjust our model and, thus, our set of differential equations is:

$$\frac{dN_C}{dt} = \frac{I\alpha}{h\nu} + \frac{n}{\tau_{cool}} - \frac{N_C}{\tau_{trap}} - \frac{N_C}{\tau_{cool}} - \frac{N_C}{\tau_{rec}} \tag{3.6}$$

$$\frac{dn}{dt}=\left(\frac{I}{h\nu}\right)^2\beta+\frac{I}{h\nu}\gamma+\frac{N_C}{\tau_{cool}}-\frac{n}{\tau_{cool}}-\frac{n}{\tau_{trap}} \tag{3.7}$$

$$\frac{dN_{trap}}{dt}=-\frac{I}{h\nu}\gamma+\frac{N_C}{\tau_{trap}}+\frac{n}{\tau_{trap}}-\frac{N_{trap}-N_{trap,final}}{\tau_{rec}} \tag{3.8}$$

with

$$\tau_{trap}=\frac{\tau_{trap,\min}}{1-\dfrac{N_{trap}}{N_{trap,\max}}} \tag{3.5}$$

and

$$I(t)=I_0\exp(-4\ln 2\frac{t^2}{\tau_p^2}) \tag{3.9}$$

Now we simulate the same group of data [see Fig. 3.5(a)] and the two results are shown in Figs. 3.9 and 3.10, fits to other experimental data are as good as these two. We also obtain the variation of τ_{trap} according to the curve of N_{trap} we have. We just need to put the simulated parameters that are needed in Eq. 3.5, along with the N_{trap} curve, then we can get the longest trap-time $\tau_{trap,\max}$. One example of τ_{trap} variation as a function of the time delay, for the pump beam power of 36.6 mW is given in Fig. 3.11. In Table 3.2, we list all the parameters for the simulation of the model with the distributed trap-time model.

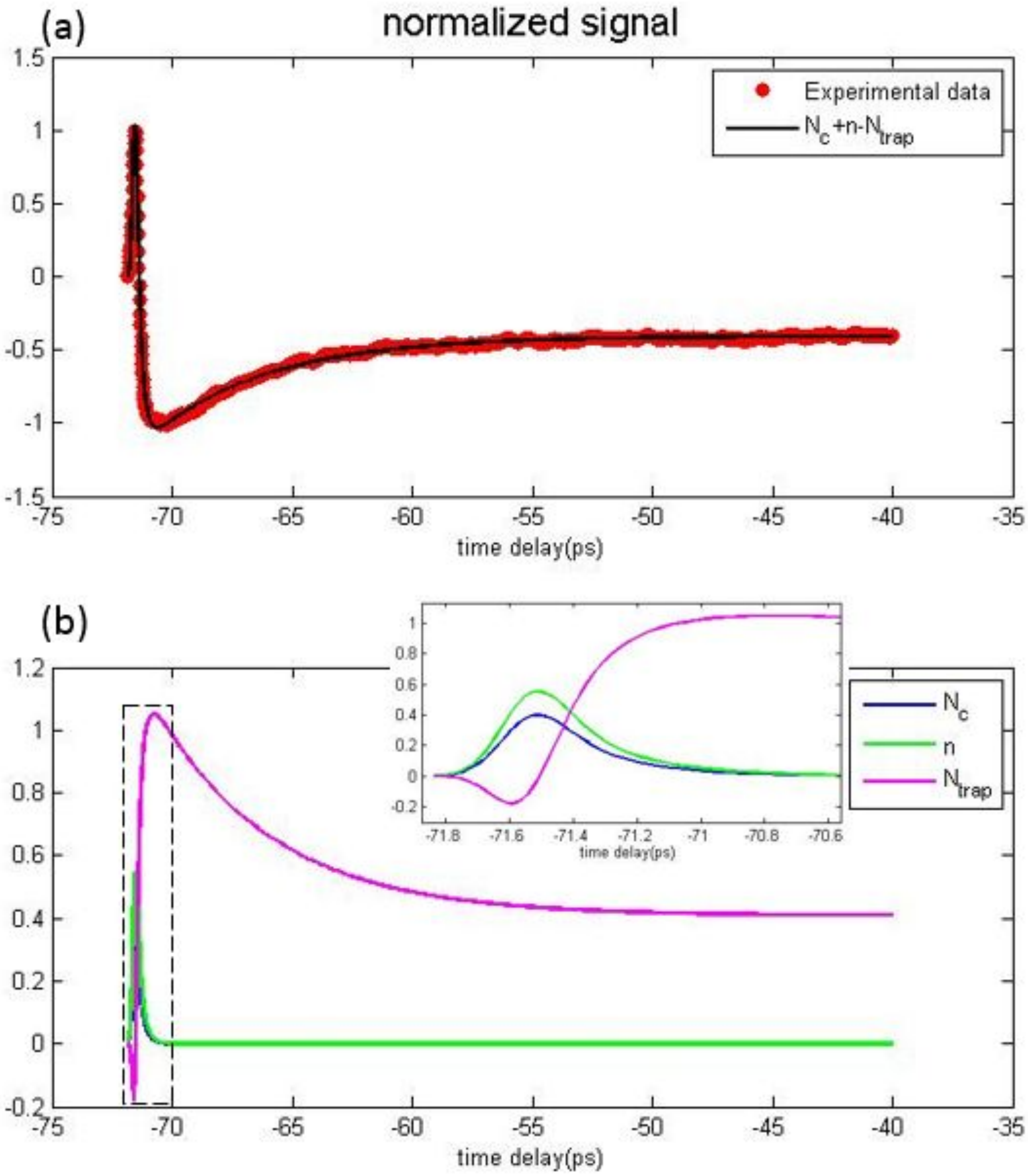

Fig. 3.9 (a) Simulation result (black line) of the model with distributed trap-time for experimental data with pump beam power of 30.8mW (red dots). (b) Corresponding numerical solutions of $N_C(t)$, $n(t)$ and $N_{trap}(t)$. The inset shows the pumping part.

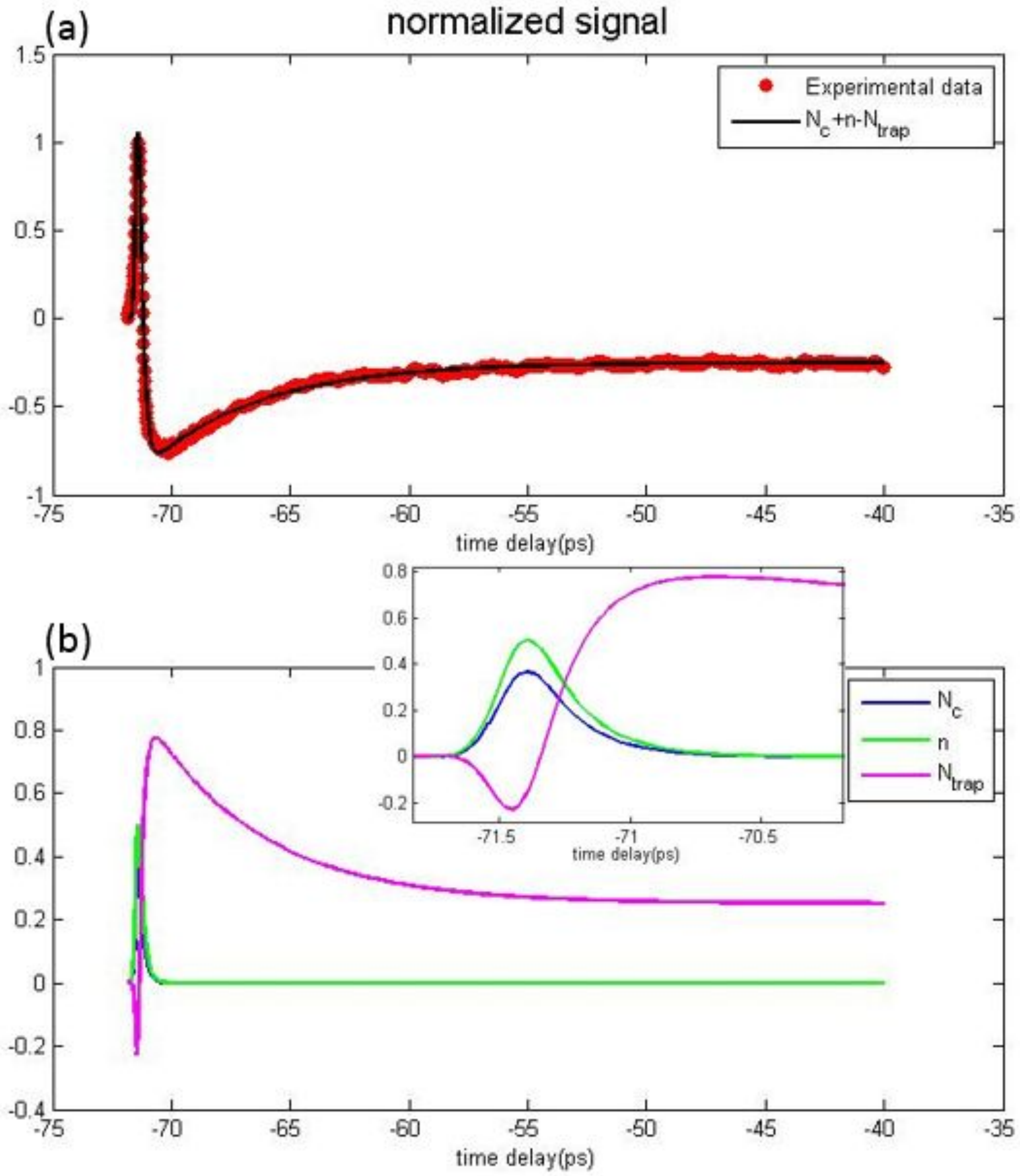

Fig. 3.10 (a) Simulation result (black line) of the model with distributed trap-time for experimental data with pump beam power of 36.6mW (red dots). (b) Corresponding numerical solutions of $N_C(t)$, $n(t)$ and $N_{trap}(t)$. The inset shows the pumping part.

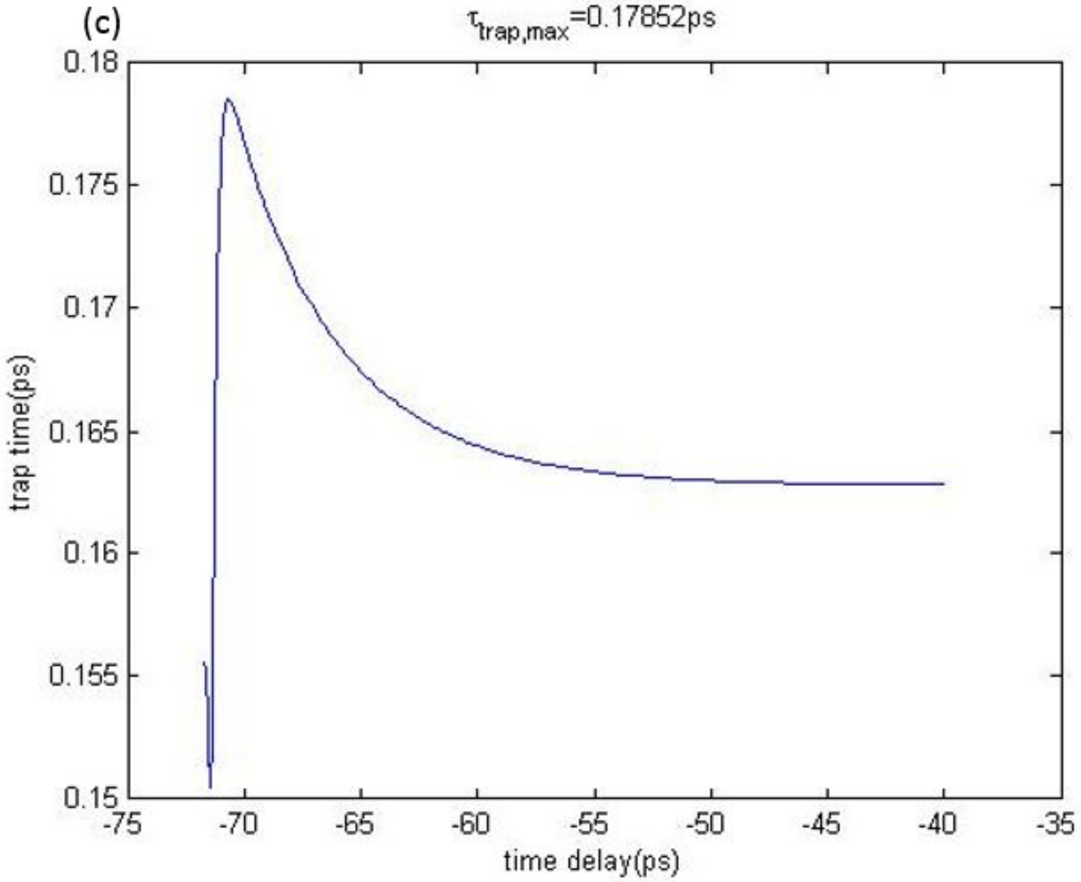

Fig. 3.11 Trap time calculated from Eq. 3.5 as a function of time delay, for experimental data with the pump power of 36.6mW.

Table 3.2 Simulation parameters from the model with distributed trap-time.

	$I\alpha$	$I^2\beta$	$I\gamma$	$\tau_{trap,\min}$ (ps)	$\tau_{trap,\max}$ (ps)	τ_{cool} (ps)	τ_{rec} (ps)
30.8 mW	4.96	0.001	7.25	0.11	0.22	7989	4.91
36.6 mW	4.04	0.001	5.19	0.15	0.18	5828	4.76
51.3 mW	5.59	0.019	4.98	0.15	0.18	5308	5.03
83.3mW	5.22	0.001	6.34	0.12	0.14	90.88	4.96
92.8mW	5.35	0.001	7.55	0.10	0.12	71.42	4.49

From the simulated $N_C(t)$, $n(t)$ and $N_{trap}(t)$ dependences [Fig. 3.9(b) and 3.10(b)], as well as Table 3.2, we can get a detailed description of the dynamic processes in the CMT sample. First of all the extremely low ratio of $I^2\beta$ refers to un-noticeable two-photon-absorption. So we could actually remove the two-photon-absorption process. The large value of $I\gamma$ means that trap-pumping plays a very important role in our CMT sample. In fact, $I\gamma$ is even slightly larger than $I\alpha$, indicating that trap-pumping is stronger than the conventional valence-to-conducting band transitions. The ultra fast τ_{trap} shows that electrons are trapped even during the process being pumped up to the conduction band. Simultaneously, the small variation range of τ_{trap} (~0.02 ps, see Fig. 3.11) indicates that there is a very large number of traps in the sample, and a single τ_{trap} used earlier (section 3.2) is a very good approximation. τ_{cool} exhibits a large variation range but it is still the slowest process, and it becomes somewhat relevant only when the largest pump beam powers are used. This is understandable because larger pump beam energy provides more photoexcited electrons, and they can scatter through electron-phonon interaction more easily, therefore resulting in shorter τ_{cool} . The final recombination time is ~5 ps, what means that in our sample the electron lifetime is short.

Chapter 4: Conclusion and future work

Through the pump-probe spectroscopy measurements described in this thesis, the carrier dynamics in as-grown CMT single crystals was analyzed by modeling simulations. Besides the basic excitation processes, the model developed by us includes such processes as trapped electron pumping, trapping of electrons, electron-phonon interaction. Traps play the most important role according to the simulation results. Trapped electron pumping and normal excitation both contribute to the excitations, while, simultaneously, no two-photon-absorption was observed. After being pumped into the excited energy states, electrons fall initially into traps with the trap-time equal to ~200 fs. There is, apparently, a large number of traps in the material, at least more than the carriers that can be excited. As the pump beam power increases, electron-phonon interaction becomes more active. The final electron-hole recombination time is ~5 ps, and some trapped electrons stay in the traps for a very long time. Overall, the photoresponse of as-grown CMT crystals is very fast (on the order on ~10 ps). Unfortunately, this, as well as the large trap concentration, are not desired for X-ray detection applications. Longer recombination time is needed in order to get longer carrier lifetime. More studies on, e.g., annealed CMT crystals are needed. Annealing should decrease the defect concentration and improve crystalline quality of CMT, leading to the increased sensitivity of X-ray detectors. Also, annealed CMT material may give longer recombination time so that longer carrier lifetime and larger $\mu\tau_e$ product can be achieved.

Another work that can be tried is two-color pump-probe spectroscopy. There are several advantages of two-color spectroscopy compared to single-color. For example, the pump beam cannot affect the detection of the probe beam so better signal-to-noise can be achieved. The dynamic processes are expected to be different as well, since very large energies of photons are likely to generate, e.g., coherent acoustic phonons in the crystal. The latter should help us understand more profoundly of the relaxation dynamics when CMT is photo-excited.

Bibliography

[1] Owens A, Peacock A. Compound semiconductor radiation detectors[J]. Nuclear Instruments and Methods in Physics Research Section A: Accelerators, Spectrometers, *Detectors and Associated Equipment*, 2004, 531(1): 18-37.

[2] Milbrath B D, Peurrung A J, Bliss M, et al. Radiation detector materials: An overview[J]. *Journal of Materials Research*, 2008, 23(10): 2561-2581.

[3] S.P. Swierkowski, G.A. Armantrout, IEEE *Trans. Nucl. Sci.* Ns-22(1975) 205

[4] G.A. Armantrout, S.P. Swierkowski, J.W. Sherohman, J.H. YEE, IEEE *Trans, Nucl. Sci.* NS-24 (1977) 121.

[5] E. Sakai, *Nucl. Instr, and Meth*, 106(1982) 121.

[6] M. Cuzin, *Nucl. Instr. and Meth*. A 253(1987) 407.

[7] J.E. Eberhardt, R.D. Ryan, A.J. Tavendale, Proc. Int. Symp. Cadium Telluride, Strasbourg, Paper No. 29, 1971.

[8] D.S. McGregor, H. Hermon, *Nucl. Instr. Meth. Phys.* Res. A 395(1997)101 124.

[9] V.F. Kushnuruk et al., Sov, *Atomic Phys.* 42 (1977) 437.

[10] F.P. Doty, J.F. Butler, J.F. Schetzina, K.A. Bowers, J. *Vac. Sci. Technol.* B 10(1990) 266.

[11] Hossain A, Yakimovich V, Bolotnikov A E, et al. Development of Cadmium Magnesium Telluride (Cd 1− x Mg x Te) for room temperature X-and gamma-ray detectors[J]. *Journal of Crystal Growth*, 2013, 379: 34-40.

[12] Sudihir B. Trivedi, Chen-Chia Wang, Susan Kutcher, Uwe Hommerich, and Witold Palosz, “Crystal Growth Technology of Binary and Ternary II-VI

semiconductors for Photonic Applications, *J. Cryst. Groth* 310(2008) 1009-1106”

[13] Giuseppe Camarda, “Characterizaiton of Detector Grade CdTeSe Crystals”, presented at the 2013 MRS Sping Meeting and Exhibit, April 1-5, 2013 April 2013.

[14] Sirenko A A, Ruf T, Cardona M, et al. Electron and hole g factors measured by spin-flip Raman scattering in CdTe/Cd 1− x Mg x Te single quantum wells[J]. *Physical Review* B, 1997, 56(4): 2114.

[15] Yasuhira T, Uchida K, Matsuda Y H, et al. Exchange interactions in CdMnTe/CdMgTe quantum wells under high magnetic fields[J]. *Physica E: Low-dimensional Systems and Nanostructures*, 2002, 13(2): 568-571.

[16] Kosyachenko L A, Mathew X, Maslyanchuk O L, et al. Optical characteristics of CdMgTe/Cu (In, Ga) Se 2 two-terminal tandem solar cell[J]. *Solar Energy*, 2015, 116: 399-406.

[17] Kosyachenko L A, Mykytyuk T I, Fodchuk I M, et al. Electrical characteristics of thin-film CdS/CdMgTe heterostructure for tandem solar cells[J]. *Solar Energy*, 2014, 109: 144-152.

[18] Mathew X, Drayton J, Parikh V, et al. Development of a semitransparent CdMgTe/CdS top cell for applications in tandem solar cells[J]. *Semiconductor Science and Technology*, 2009, 24(1): 015012.

[19] P. F. Moulton, J. Opt. Soc. Am. B 3, 125-133 (1986).

[20] M. Fermann, A. Galvanaouskas, and G. Sucha, Ultrafast Lasers: Technology and Applications. CRC Press (2003).

[21] D. Spence, P. Kean, et al., *Optics Letters* 16(1), 42 (1991).

[22] J. Jin and S. Kim, Advances in Solid State Lasers Development and Applications, INTECH, (2010).

[23] Andreas Othonos, "Probing Ultrafast Carrier and phonon Dynamics in Semiconductors", J. *Appl. Phys*., vol. 83, pp. 1789-1828, 1998.

[24] Jagdepp Shah, Ultrafase Spebtroscopy of Semiconductors and Semiconductor Nanostructures (Springer, 1996), Chap. 1.

[25] Fushitani M. Applications of pump-probe spectroscopy[J]. Annual Reports Section" C"(Physical Chemistry), 2008, 104: 272-297.

[26] Coherent, Inc,. "Coherent Mira Model 900 Laser Operator's Manual", 1991.

[27] Coherent, Inc., "Verdi V-8/V-10 Lasers Operator's Manual", 1999.

[28] Stanford Research Systems, "Model SR830 DSP Lock-in Amplifier", 2011.

[29] Szeles C, Driver M C. Growth and properties of semi-insulating CdZnTe for radiation detector applications[C]//SPIE's International Symposium on Optical Science, Engineering, and Instrumentation. International Society for *Optics and Photonics*, 1998: 2-9.

[30] M. C. Downer and C. V. Shank, *Phys. Rev. Lett.* 56, 761 (1986).

[31] F. E. Doany and D. Grischkowsky, *Appl. Phys. Lett.* 52, 36 (1988).

[32] P. Uhd Jepsen, W. Schairer, I. H. Libon, U. Lemmer, N.E. Hecker, M. Birkholz, K. Lips, M. Schall, *Appl. Phys. Lett* 79/9 (2001) 1291.

[33] S. D. Benjamin, H. S. Loka, A. Othonos, and P. W. E. Smith, *Appl. Phys, Lett.* 68 (1996) 2544.

Appendix

1. Defined models on relaxation processes

1.1. Model that includes all the processes (correspond to Eq. 3.1; Eq. 3.2; Eq. 3.4)

```
%This model includes all the dynamic processes with trap time as constant.
%The first equation is for the electrons in the conduction band.
%The second equation is for the hot electrons.
%The third equation is for the electrons fall into trap sites.
%k(1) is I0*alpha
%k(2) is I0^2*beta
%k(3) is -4ln2/(taop)^2
%k(4) is b
%k(5) is tau_trap
%k(6) is tau_rec
%k(7) is tau_cool
%k(8) is I0*gamma
%k(9) is the final trap concentration
%-----------------------------------------------------
```

```
----------------
    function[dNdt]=model2_detail(t,N,k)

    dNdt=zeros(3,1);
    dNdt(1)=k(1)*exp(k(3)*(t-k(4))^2)-N(1)*(1/k(5))+N(2)*(
1/k(7))-N(1)*(1/k(7))-N(1)*(1/k(6));
    dNdt(2)=k(2)*(exp(k(3)*(t-k(4))^2))^2+k(8)*exp(k(3)*(t
-k(4))^2)+N(1)*(1/k(7))-N(2)*(1/k(7))-N(2)*(1/k(5));
    dNdt(3)=N(1)*(1/k(5))+N(2)*(1/k(5))-k(8)*exp(k(3)*(t-k
(4))^2)-(N(3)-k(9))*(1/k(6));
    end
```

1.2. Model with distributed trap time

```
    %This model make the trap sites as limited numbers so the
trap time would
    %be ditributed.
    %The first equation is for the electrons in the conduction
band.
    %The second equation is for the hot electrons.
    %The third equation is for the electrons fall into trap
sites.
```

```
%k(1) is I0*alpha
%k(2) is I0^2*beta
%k(3) is -4ln2/(taop)^2
%k(4) is b
%k(5) is tau_trap,min
%k(6) is tau_trap,min*Ntrap,max
%k(7) is tau_rec
%k(8) is tau_cool
%k(9) is I0*gamma
%k(10) is the final trap concentration
%1/tau_trap=(1/k(5)-N(3)*1/k(6))
%-------------------------------------------------------
function[dNdt]=distribute_trp_tm(t,N,k)

dNdt=zeros(3,1);
dNdt(1)=k(1)*exp(k(3)*(t-k(4))^2)-N(1)*(1/k(5)-N(3)*1/k(6))+N(2)*(1/k(8))-N(1)*(1/k(8))-N(1)*(1/k(7));
dNdt(2)=k(2)*(exp(k(3)*(t-k(4))^2))^2+k(9)*exp(k(3)*(t-k(4))^2)+N(1)*(1/k(8))-N(2)*(1/k(8))-N(2)*(1/k(5)-N(3)*1/k(6));
dNdt(3)=(N(1)+N(2))*(1/k(5)-N(3)*1/k(6))-k(9)*exp(k(3)*(t-k(4))^2)-(N(3)-k(10))*(1/k(7));
```

```
end
```

1.3. Model without two-photon-absorption, and with distributed trap time

```
%This model doesn't include two photon absoption.

%First equation is for electrons in conduction band.

%Second equation is for hot electrons

%Third equation is for electrons in trap sites.

%k(1) is I0*alpha

%k(2) is final trap concentration

%k(3) is -4ln2/(taop)^2

%k(4) is b

%k(5) is tau_trap,min

%k(6) is tau_trap,min*Ntrap,max

%k(7) is tau_rec

%k(8) is tau_cool

%k(9) is I0*gamma

%1/tau_trap=(1/k(5)-N(3)*1/k(6))




%-----------------------------------------------------

function[dNdt]=model_no2pa(t,N,k)
```

```
    dNdt=zeros(3,1);
    dNdt(1)=k(1)*exp(k(3)*(t-k(4))^2)-N(1)*(1/k(5)-N(3)*1/k(6))+N(2)*(1/k(8))-N(1)*(1/k(8))-N(1)*(1/k(7));
    dNdt(2)=k(9)*exp(k(3)*(t-k(4))^2)+N(1)*(1/k(8))-N(2)*(1/k(8))-N(2)*(1/k(5)-N(3)*1/k(6));
    dNdt(3)=(N(1)+N(2))*(1/k(5)-N(3)*1/k(6))-k(9)*exp(k(3)*(t-k(4))^2)-(N(3)-k(2))*(1/k(7));
    end
```

2. Numerical simulation of the measured signal

2.1. Simulation function

```
    function [ Ti ] = numvalue( k,xdata )
    %To get the numerical solutions of model equations at one set of k values
    %which are used in the comparison with measured signals.
    y0 =  0; % ydata(1), already set to be zero;
    T0=[y0 , y0 , y0];
    %[~, T]=ode45(@model2_detail,xdata,T0,[],k);
    [~, T]=ode45(@model_no2pa,xdata,T0,[],k);
    %[~, T]=ode45(@model_2pa_trp_tm,xdata,T0,[],k);
    %[~, T]=ode45(@distribute_trp_tm,xdata,T0,[],k);
```

```
    %[~, T]=ode45(@model1,xdata,T0,[],k);
    %solve the equations and get solutions,choose according
to the model in use
    Ti=T(:,1) + T(:,2) - T(:,3);%N_con+N_hot-N_trap
    end
```

2.2. Signal loading, requirements setting and simulation function calling

```
    clear
    xdata=xlsread('92.8mw.xlsx','A62:A722');
    ydata=xlsread('92.8mw.xlsx','J62:J722');
    %load measured signal in use
    ydata=smooth(smooth(ydata));
    ydata=ydata-ydata(1); %shift first point to zero
    ydata=ydata/max(ydata);

    options=optimset('TolFun',1e-8,'TolX',1e-8,'MaxFunEval
s',50000,'MaxIter',5000,'Algorithm','trust-region-reflect
ive','Display','iter');
    %set option functions to limit the simulation

    %model2_detail
```

```
   %I0*alpha   I0^2*beta   -4ln2/(taop)^2   b
tao_trap,hot      tao_rec   tao_cool     I0*gamma  final
trap
   %k0=[5        5        -69.3        -71.5      0.8
10       600          3       0.4];
   %ub=[10000    100        -64         -70.5     100
10       1000        1000      1];
   %lb=[0.1       0.01        -71       -72.5     1e-7
1e-4      1e-4         0.1       0.01];

   %model_no2pa
   %I0*alpha     final trap   -4ln2/(taop)^2    b
tau_trap,min    tau_trap,min*Ntrap,max   tau_rec
tau_cool    I0*gamma
   k0=[10           0.4         -69.3       -71.5     0.8
0.4              4.9      600         1];
   ub=[10000        1         -65          -70.5    100
1                1000     10000        1000];
   lb=[0.1          0.01        -71          -72.5   1e-7
1e-7              1e-4     1e-4         0.1];

   %model_2pa_trp_tm
```

```
   %I0*alpha      I0^2*beta   -4ln2/(taop)^2  b
tao_trap,min       tao_rec     I*gamma     final trap
   %k0=[5            5         -69.3       -71.5      0.8
4.4           1          0.4];
   %ub=[10000        100        -64        -70.5
100        1000        1000         1];
   %lb=[0.1           0.01        -125       -72
1e-4        1e-4        0.1        0.01];

   %distribute_tp_tm
   %I0*alpha     I0^2*beta    -4ln2/(taop)^2    b
tau_trap,min   tau_trap,min*Ntrap,max   tau_rec
tau_cool    I0*gamma     final trap
   %k0=[10           5          -69.3        -273    0.4
0.4              120       600         1           0.4];
   %ub=[10000        100         -65         -272     100
1              10000     10000         1000          1];
   %lb=[0.1          1e-8        -71        -273    1e-7
1e-7             1e-4     1e-4         0.1          0.01];
   %Set the initial values, upper bounds and lower bounds for
the parameters (k series)
```

```
    k=lsqcurvefit(@numvalue,k0,xdata,ydata,lb,ub,options);
%fit the solutions with the measured signal
```

3. Test and plot

```
    T0=[0,0,0];
    %[tt,T]=ode45(@model2_detail,[xdata(1)xdata(length(xda
ta))],T0,[],k);
    [tt,T]=ode45(@model_no2pa,[xdata(1)
xdata(length(xdata))],T0,[],k);
    %[tt,T]=ode45(@model_2pa_trp_tm,[xdata(1)xdata(length(
xdata))],T0,[],k);
    %[tt,T]=ode45(@distribute_trp_tm,[xdata(1)xdata(length
(xdata))],T0,[],k);
    %[tt,T]=ode45(@model1,[xdata(1)
xdata(length(xdata))],T0,[],k);
    %solve the equation set using the best fit K series, choose
due to the model in use
    Tt1=T(:,1);
    Tt2=T(:,2);
    Tt3=T(:,3);
    Tt4=T(:,1)+T(:,2)-T(:,3);
```

```
subplot(211);

plot(xdata,ydata,'.r');

xlabel('time delay(ps)');

title('normalized signal','fontsize',16);

hold on;

%plot normalized signal


plot(tt,Tt4,'black');

legend('Experimental data','N_c+N_h-N_t');

%plot simulation result


subplot(212);

plot(tt,Tt1,'blue')

hold on

plot(tt,Tt2,'green')

hold on

plot(tt,Tt3,'m')

legend('N_c_o_n','N_h_o_t','N_t_r_a_p');

xlabel('time delay(ps)');

%plot N_con, N_hot and N_trap
```

4. Calculation of $\tau_{trap,\max}$

```
trap=k(6)./(k(6)./k(5)-Tt3); %trap time equation

top=max(trap);%the longest trap time

plot(tt,trap);

xlabel('time delay(ps)');

ylabel('trap time(ps)');

title(['\tau_t_r_a_p_,_m_a_x=',num2str(top),'ps']);
```